

Over-the-Air Goal-Oriented Communications

Kyriakos Stylianopoulos
Paolo Di Lorenzo
George C. Alexandropoulos

Goal-oriented communications offer an attractive alternative to the Shannon-based communication paradigm, where the data is never reconstructed at the Receiver (RX) side. Rather, focusing on the case of edge inference, the Transmitter (TX) and the RX cooperate to exchange features of the input data that will be used to predict an unseen attribute of them, leveraging information from collected data sets. This chapter demonstrates that the wireless channel can be used to perform computations over the data, when equipped with programmable metasurfaces. The end-to-end system of the TX, RX, and MS-based channel is treated as a single deep neural network which is trained through backpropagation to perform inference on unseen data. Using Stacked Intelligent Metasurfaces (SIM), it is shown that this Metasurfaces-Integrated Neural Network (MINN) can achieve performance comparable to fully digital neural networks under various system parameters and data sets. By offloading computations onto the channel itself, important benefits may be achieved in terms of energy consumption, arising from reduced computations at the transceivers and smaller transmission power required for successful inference.

Kyriakos Stylianopoulos
Department of Informatics and Telecommunications, National and Kapodistrian University of Athens, Greece, e-mail: kstylianop@di.uoa.gr

Paolo Di Lorenzo
National Inter-University Consortium for Telecommunications (CNIT), Parma, Italy and DIET Department, Sapienza University of Rome, Rome, Italy, e-mail: paolo.dilorenzo@uniroma1.it

George C. Alexandropoulos
Department of Informatics and Telecommunications, National and Kapodistrian University of Athens, Greece, e-mail: alexandg@di.uoa.gr

1 Introduction

The rapid proliferation of connected devices, driven by the Internet of Things (IoT) paradigm, has made massive Machine-Type Communications (mMTC) a cornerstone of Fifth Generation (5G) networks [1]. Looking toward Sixth Generation (6G) systems and beyond, the focus is shifting towards realizing ultra low latency and energy-efficient Device-to-Device (D2D) wireless links. This necessitates a fundamental reconsideration of the PHYSical (PHY) layer design, calling for innovations in power- and cost-efficient hardware combined with significant advancements in information processing algorithms [2]. To manage the enormous volume of IoT-generated data, which includes signals used for positioning and sensing, processing at the network edge is becoming essential. 6G is thus envisioned to embrace a cross-layer design, blurring the traditional boundaries between the user plane and the PHY layer. This data-driven trend promotes Edge Inference (EI) [3] and Goal-Oriented Communications (GOC) [4].

In this new paradigm, the Transmitter (TX) sends data not for perfect reconstruction at the Receiver (RX), but to enable the RX to extract information necessary for a specific network task. EI is a specialized form of this approach, focusing on enabling the RX to infer a target feature from the transmitted symbol using patterns learned from past input-target examples. This offers dual benefits: reduced computational complexity at the RX (by avoiding full data reconstruction) and efficient use of communication resources (by encoding only task-relevant information). Machine Learning (ML) tools [5], particularly Deep Neural Networks (DNNs) [6, 7, 8, 9], are gaining traction for IoT applications at the network edge in 6G [10, 11]. They offer a data-driven alternative to traditional model-based approaches, which often rely on unrealistic assumptions. ML excels at identifying and exploiting complex patterns that accurately reflect the deployment environment. Moreover, the heavy computational load associated with ML is typically confined to the offline training phase, enabling low latency computations during deployment. However, a major obstacle for EI is the hardware complexity and resulting power consumption. The efficient execution of DNN computations relies heavily on parallel processing units, which substantially increase energy demands at the edge. A truly transformative concept proposes that computational tasks need not be restricted solely to digital transceivers. By developing GOC based on smart wireless environments [12, 13], the wireless channel can be transformed from a passive medium into an active computational entity [14, 15].

This is made possible through the use of (programmable) Meta-Surfaces (MSs). Those near-ElectroMagnetic (EM)-passive structures, deployed as Reconfigurable Intelligent Surfaces (RISs) for controlled reflection [16, 17], or as Stacked Intelligent Metasurfaces (SIM) [18, 19, 20] at the TX/RX for extremely large apertures [21], offer controllable wave transformations [22]. Traditionally, such MS technologies have been developed for low complexity and energy efficient signal strength amplification in communication and sensing applications [23, 24, 25, 26, 27]. By shaping the propagating EM waves Over-the-Air (OTA) using passive or analog operations, these systems can execute portions of feature extraction, compression, or filtering

with almost zero energy consumption. This process effectively offloads computational tasks from conventional, energy-hungry digital hardware into the PHY layer itself, paving the way for sustainable and ultra-efficient ML-enabled systems and EI applications [14].

In this context, this chapter explores the joint exploitation of MSs and conventional wireless effects to realize computations analogous to those performed by DNNs. This approach allows the entire End-to-End (e2e) MS-parametrized Multiple-Input Multiple-Output (MIMO) system to be treated as a single DNN, composed of digital, analog, and wave-domain layers of computation, offering a significant reduction in the complexity and power requirements for IoT devices performing EI.

2 Preliminaries of Goal-Oriented Communications

2.1 Probabilistic Inference

The objective of an inference task is to determine a target attribute \mathbf{o} from a given input observation \mathbf{x} , represented by the unknown mapping $\mathbf{o} = l(\mathbf{x})$. Since an analytical form for $l(\mathbf{x})$ is intractable, this relationship is approximated using a dataset of input-target pairs, $\mathcal{D} \triangleq \{(\mathbf{x}_i, \mathbf{o}_i)\}_{i=1}^{|\mathcal{D}|}$. From a probabilistic perspective, solving the inference problem involves fitting the conditional probability density function (PDF) $p(\mathbf{o}|\mathbf{x})$ to the data. However, in most practical scenarios, only point estimates are required, reducing the task to predicting the most probable target value ($\hat{\mathbf{o}}$) for a given observation \mathbf{x} .

In the ML paradigm, this approximation is handled by a parametrized model: $\hat{\mathbf{o}} \triangleq f_{\mathbf{w}}(\mathbf{x})$. The parameter values \mathbf{w} are optimized by minimizing an amortized cost function, $J(\mathbf{w})$, averaged over all training instances in \mathcal{D} :

$$J(\mathbf{w}) \triangleq \frac{1}{|\mathcal{D}|} \sum_{i=1}^{|\mathcal{D}|} \mathfrak{J}(\mathbf{o}_i, \hat{\mathbf{o}}_i), \quad \text{where } \hat{\mathbf{o}}_i = f_{\mathbf{w}}(\mathbf{x}_i). \quad (1)$$

The per-instance cost, $\mathfrak{J}(\mathbf{o}_i, \hat{\mathbf{o}}_i)$, quantifies the prediction error and often has a direct probabilistic interpretation [28, 29]:

- **Classification:** For tasks where the input is assigned to one of d_{cl} classes (target \mathbf{o} is one-hot encoded, i.e., \mathbf{o} is a d_{cl} -sized vector containing zeros everywhere except for the element and the index of the input class which contains one), the standard choice is the Cross Entropy (CE) loss function:

$$\mathfrak{J}_{\text{CE}}(\mathbf{o}_i, \hat{\mathbf{o}}_i) \triangleq - \sum_{j=1}^{d_{\text{cl}}} [\mathbf{o}_i]_j \log [\hat{\mathbf{o}}_i]_j. \quad (2)$$

Minimizing \mathfrak{J}_{CE} is mathematically equivalent to performing maximum likelihood estimation of the model parameters (\mathbf{w}) under the assumption that the conditional PDF $p(\mathbf{o}|\mathbf{x})$ follows a multivariate Bernoulli distribution.

- **Regression:** For continuous target predictions, where $\mathbf{o}, \hat{\mathbf{o}} \in \mathbb{R}^{d_{\text{out}} \times 1}$, the common Mean Squared Error (MSE) metric $(1/d_{\text{out}} \|\mathbf{o} - \hat{\mathbf{o}}\|^2)$ is typically used. The use of MSE implies the assumption that the conditional PDF $p(\mathbf{o}|\mathbf{x})$ is a Gaussian distribution.

2.2 Artificial Neural Networks

While a broad spectrum of parametrized function families is available for modeling $f_{\mathbf{w}}(\cdot)$, the current cutting edge in inference relies heavily on DNNs. These networks are favored due to their remarkable expressivity, a wide array of specialized architectural components tailored to various tasks, and the inherent parallelizability of their computations, which allows for real-time inference on modern hardware. Mathematically, a neural network is defined as a composition of L layers:

$$f_{\mathbf{w}}(\mathbf{x}) \triangleq f_{\mathbf{w}^L}^L \left(f_{\mathbf{w}^{L-1}}^{L-1} \left(\dots f_{\mathbf{w}^1}^1(\mathbf{x}) \dots \right) \right), \quad (3)$$

where the l -th layer ($l = 1, 2, \dots, L$) is governed by parameters \mathbf{w}_l . The output of layer l , denoted by $\bar{\mathbf{o}}^l$, serves as the input to the subsequent $(l+1)$ -th layer, yielding the recursive definition $\bar{\mathbf{o}}^l \triangleq f_{\mathbf{w}^l}^l(\bar{\mathbf{o}}^{l-1})$. The network begins with the observation, $\bar{\mathbf{o}}^0 = \mathbf{x}$. For notational simplicity, the complete set of parameters is aggregated as $\mathbf{w} \triangleq [\mathbf{w}_1^\top, \mathbf{w}_2^\top, \dots, \mathbf{w}_L^\top]^\top$.

We will not go deeper into the specific details of individual layer functions here, acknowledging the extensive body of research dedicated to developing specialized layers that efficiently perform data-specific computations and extract high-level patterns from training sets [29]. Nonetheless, a crucial requirement is that each layer function $f_{\mathbf{w}^l}^l(\cdot)$, must incorporate a non-linear element. Historically, these nonlinearities were often discriminatory or sigmoidal [30]. These properties are foundational to the *universal approximation theorem*, which guarantees that artificial neural networks comprising at least two layers (and potentially infinite width) can approximate any arbitrary mapping $\mathbf{o} = l(\mathbf{x})$, thus achieving $f_{\mathbf{w}}(\mathbf{x}) \cong l(\mathbf{x})$ [30].

Beyond these theoretical assurances, the practical task of determining the optimal parameter values \mathbf{w} for successful inference can be solved efficiently. This involves substituting the neural network expression from (3) into the appropriate cost function (e.g., (2) for classification) and then into the amortized loss function (1). This minimization problem is typically tackled using variants of the Stochastic Gradient Descent (SGD) method. The core mechanism is the computation of gradients $\partial J(\mathbf{w})/\partial \mathbf{w}$ by leveraging the chain rule to propagate error signals backward through the network layers. This procedure defines the renowned *backpropagation* algorithm [31, 32], which is the central computational method underpinning deep learning.

2.3 Edge Inference

The emerging field of EI involves the deployment and training of inference tasks across a wireless communication infrastructure. We consider an uplink scenario where a multi-antenna TX observes the input \mathbf{x} and aims to communicate its estimate $\hat{\mathbf{o}}$ of the target attribute \mathbf{o} to a remote RX. Initially, this process appears achievable under two established communication paradigms:

“Infer-then-transmit”: In this option, the TX first computes the target estimate $\hat{\mathbf{o}} = f_{\mathbf{w}}(\mathbf{x})$ locally. It then prepares the transmission signal \mathbf{s} by applying source coding (data compression) and channel coding (modulation and beamforming) to $\hat{\mathbf{o}}$. These coding steps are necessary to ensure the system achieves a satisfactory communication rate, enabling the RX to successfully reconstruct $\hat{\mathbf{o}}$ via decoding and decompression. Implementing these operations in high complexity modern wireless systems often requires dedicated optimization procedures and accurate Channel State Information (CSI), incurring extra computational costs. While inference targets are typically of a much smaller dimension than the original observations, leading to small rate requirements, this approach burdens the TX with the cost of executing DNN computations locally. This hardware assumption is often overly optimistic for IoT or other lightweight devices envisioned for EI tasks, which are constrained by low complexity and minute power consumption.

“Transmit-then-infer”: The converse approach bypasses local DNN-based EI at the TX. Instead, the TX performs only source and channel coding on the original observation \mathbf{x} , which is then transmitted over the link. Subsequently, the RX decodes the received signal to obtain the input data point and then feeds it into its local $f_{\mathbf{w}}(\cdot)$ to perform inference. Although the RX is typically assumed to possess sufficient power and hardware capacity to support a DNN in uplink settings, transmitting the entire original observation \mathbf{x} often imposes high link budget demands that may be difficult to satisfy. A flexible alternative to mitigate the trade-offs of the above options is possible by exploiting the sequential nature of the DNN structure defined in (3) [33]. This leads to the following EI paradigm:

“Infer-while-transmitting” (DNN splitting): Intermediate representations, $\bar{\mathbf{o}}^l$ for $l = 1, 2, \dots, L-1$, can be constructed with arbitrary dimensions. Architectural design often includes one or more small-sized *bottleneck layers* (as seen in auto-encoders [34] and U-Nets [35]), which effectively perform compression to preserve only the most relevant information. Leveraging this, one can partition the DNN such that the first $L' < L$ layers reside at the TX. The output $\bar{\mathbf{o}}^{L'}$ is then transmitted over the network and passed sequentially to the remaining layers, from $(L'+1)$ up to L , at the RX.

The latter paradigm is clearly the most flexible, allowing for dynamic balancing of the computational load and communication resources between the TX and RX. The initial application of DNNs in transceivers was studied under the Joint Source Channel Coding (JSCC) paradigm [36, 37]. Unlike Shannon’s separation theorem, which treats source and channel coding separately [38], JSCC develops joint encoders and decoders that account for channel conditions to achieve superior reconstruction performance. However, JSCC’s objective is limited strictly to data reconstruction.

Conversely, Deep Semantic Communications (DeepSC) approaches [39] aim to transmit the meaning of the data, quantified by cost functions defined by various GOC objectives. For example, the DeepSC architecture of the work in [40] uses separate source and channel sub-modules. While its channel encoder/decoder maximizes a difficult-to-evaluate Mutual Information (MI) objective, this maximization negates the channel's effects rather than leveraging them for computation. Similarly, a separate source/channel coding approach for image retrieval [41] showed benefits but also treated the channel purely as a source of noise. The concept of DNN splitting for EI [33, 42] has been investigated from an information bottleneck perspective to determine optimal network partitioning in uncontrollable wireless channels. This framework, which transmits intermediate feature representations, aligns well with the broader GOC objective.

2.4 Computational Considerations

When implementing DNN splitting over a wireless channel characterized by realistic effects (i.e., large- and small-scale fading, and Additive White Gaussian Noise (AWGN)), the transmitted intermediate output $\bar{o}^{L'}$ from the L' -th DNN layer will inevitably be distorted upon arrival at the RX. Representing the channel state via an abstract random variable \mathcal{H} , the training objective remains the minimization of the w -parametrized cost function $J(w)$, but must now account for the stochastic nature of the wireless environment:

$$O\mathcal{P}_{EI} : \min_w \mathbb{E}_{\mathcal{H}}[J(w)],$$

where the value of the objective function is instantaneously affected by distortion induced by each channel realization.

Assuming sufficient wireless channel capacity, the standard paradigm of wireless communications suggests that optimizing both endpoints for source and channel encoding/decoding will effectively eliminate the distortion on the received $\bar{o}^{L'}$. The resulting decoded output can then be directly fed into the network's $(L' + 1)$ -layer as if the channel were not present; the channel is effectively *hidden* from the neural network's processing perspective. This reconstruction-centric approach aligns with the traditional practices of both wireless communications and ML, and it has successfully exhibited satisfactory results [40, 43]. However, optimizing the system primarily for signal reconstruction may result in unnecessary computational overheads due to the following considerations:

1. EI's primary objective is the calculation of an arbitrary function of the input, not the perfect reconstruction of intermediate variables. From this viewpoint, devoting resources to reconstructing intermediate variables is not always the most efficient path. GOC can be viewed as a specialized instance of lossy compression between the unseen target \mathbf{o} and its estimation $\hat{\mathbf{o}}$, where $\mathfrak{J}(\mathbf{o}, \hat{\mathbf{o}})$ acts as the distortion metric. Information-theoretic perspectives, such as those studying variations of

the distortion-rate function [44], indicate that the channel rate necessary to meet a desired error threshold for transmitting intermediate variables is typically less than the channel capacity required for reconstruction with arbitrarily small error probabilities.

2. From an engineering standpoint, perfect reconstruction may not be necessary, as the subsequent neural network layers are often inherently designed to tolerate noisy inputs, reflecting the stochastic nature of inference problems. Furthermore, deliberately injecting noise into layer activations during training [45, 46] and inference [47, 48] is a recognized technique for enhancing model regularization and uncertainty estimation.
3. The wireless channel, which inherently acts as a stochastic function on the transmitted data, imposes its own computations. While this channel function is generally not controllable by the e2e system, Over-the-Air Computation (OAC) methods exploit the superimposition property of wireless signals to implement certain classes of computational functions directly on the propagation medium. Crucially, the controllability introduced by emerging MS technologies has the potential to enable more sophisticated OAC, effectively offloading computation away from the communication network endpoints. Notice that, in this book, we differentiate OAC from “AirComp,” as defined in [49], which strictly addresses nomographic functions requiring predefined analytical functions at transceivers for computation, primarily applied in multiple access and federated learning. Our use of OAC refers to any effects of the propagation environment on signals that are controllable and leveraged toward a specific computational goal.

3 Deep Diffractive Neural Networks

3.1 Basic Principles of Diffractive Computing

The primary technology enabling the wave domain implementation of DNNs is the concept of SIM [18]. A SIM consists of densely arranged, thin layers of diffractive MSs, where each MS layer is composed of multiple unit elements offering tunable EM responses. The complete SIM structure is typically housed within absorbing material, negating multipath effects. By precisely controlling the EM responses of the unit elements, specific linear operations can be executed on the signals propagating from the initial MS layer. Consider a SIM device comprising M layers of diffractive MSs, each containing $N_m = N_m^{\text{vert}} N_m^{\text{hor}}$ elements arranged into N_m^{hor} columns and N_m^{vert} rows ($m = 1, \dots, M$), as depicted in Fig. 1. The element-to-element propagation between consecutive SIM layers is governed by geometric optics due to their dense placement [18, 50, 51]. Given elements n and n' ($1 \leq n, n' \leq N$) with distance $d_{n,n'}$ and area S_M from layers m and $m-1$ ($2 \leq m \leq M$), the propagation matrix $\Xi_m \in \mathbb{C}^{N \times N}$ is given via the Rayleigh-Sommerfeld diffraction equation [52, 18]:

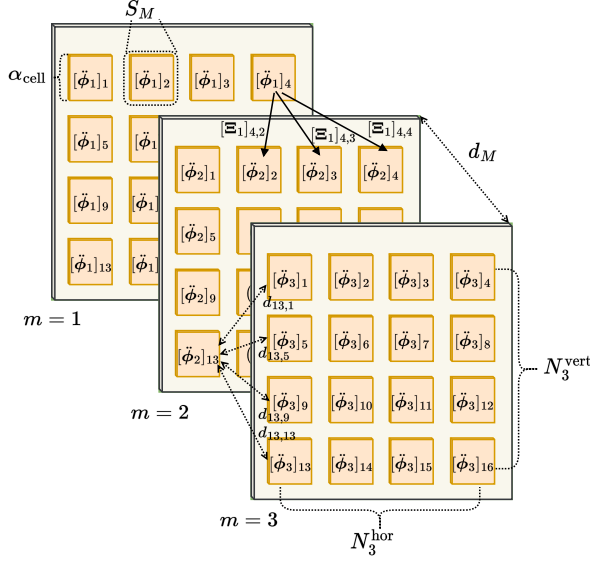
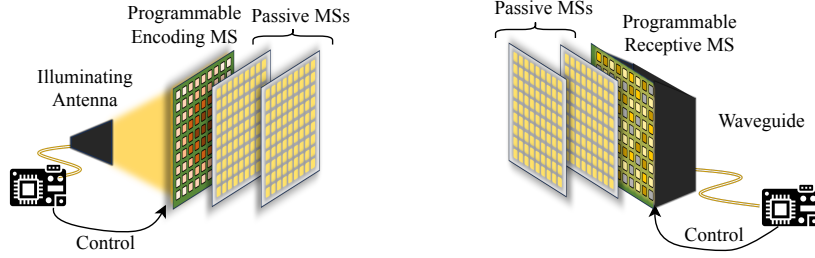


Fig. 1: A SIM of $M = 3$ layers, each with $N_m = 16$ elements, that is used as a Deep Diffractive Neural Network (D²NN) for wave-domain-based ML. The controllable responses $[\phi_m]_n$ ($m = 1, \dots, M$ and $n = 1, \dots, N$) are treated as trainable DNN weights.

$$[\Xi_m]_{n,n'} \triangleq \frac{d_M S_M}{d_{n,n'}^2} \left(\frac{1}{2\pi d_{n,n'}} - \frac{J}{\lambda} \right) \exp(J2\pi d_{n,n'}), \quad (4)$$

where λ is the carrier frequency and $J \triangleq \sqrt{-1}$ is the imaginary unit. The responses of the unit elements of the m -th layer \mathbf{v}_l are modeled as typical idealized unit-amplitude phase shifters, i.e., $[\phi_m]_n \triangleq \exp(J\xi_{m,n})$, where $\xi_{m,n}$ is the controllable phase shift. It is important to highlight that, in deriving the exact form of (4), it is necessary to assume that the width of each MS element is negligible to the layer-to-layer distance d_M , which provides a limit on how densely stacked the SIM layers might be so that they are accurately modeled through this approach. Considering that the width of each rectangular element is typically set to $\lambda/2$ (i.e., $S_M = \lambda^2/4$), a rule of thumb is to set $d_M \geq 5\lambda$ to satisfy this assumption. Contrarily, placing SIM layers at uncharacteristically large distances, say $d_M \geq 10\lambda$, induces large attenuation as it can be observed by the $d_{m,m'}^3$ factor at the denominator of (4), and may thus decrease the effectiveness of the overall SIM device.

By letting $\ddot{\Phi}_m(t) \triangleq \text{diag}(\ddot{\phi}_m(t))$, the overall SIM response matrix is mathematically expressed as [53]:



(a) A programmable MS acting as the input layer. The values of the input data vector (or matrix) are encoded as the phase responses of the MS elements and a directive antenna provides a beacon (i.e., non-information bearing) signal that illuminates the backplate of the first layer to initiate the forward pass.

(b) An MS whose elements fully absorb the impinging signals acting as the output layer. The responses of the elements may be controllable and, therefore, adopted waveguide(s) at the backplate perform weighted summations on the received signals to reduce the resulting number of Radio-Frequency (RF) chains needed for obtaining the output of the D²NN in the digital domain.

Fig. 2: Illustration of techniques for transferring digital data to and from the RF domain using programmable MSs as the first and last D²NN layers. Once training is complete, unit cells characterized by the obtained responses for intermediate SIM layers may be manufactured to be completely passive, providing important benefits in terms of energy consumption during wave computation.

$$\ddot{\Phi}(t) \triangleq \left(\prod_{m=M}^2 \ddot{\Phi}_m(t) \Xi_m \right) \ddot{\Phi}_1(t) \in \mathbb{C}^{N_m \times N_m}, \quad (5)$$

where the input values may be encoded at the responses of $\ddot{\Phi}_1(t)$ and $\ddot{\Phi}_M(t)$ may play the role of the output vector at the RX.

Since the latter operations are linear with respect to the impinging signal at each layer, and because every element in one layer contributes to the signal arriving at every element of the subsequent layer, this architecture bears a close resemblance to a DNN's fundamental building block: the fully connected linear layer. Leveraging this resemblance, D²NNs can be physically realized by treating the SIM responses as the trainable weights of the network [52, 54].

A prerequisite for D²NNs is that the input data must be available in the RF domain. This requirement is inherently satisfied when the D²NN is employed for processing ambient RF signals in sensing applications. This offers significant advantages over digital DNNs in terms of energy efficiency and latency, as it eliminates the need for analog to digital conversions. Conversely, when a D²NN performs inference on digital input data, the conversion to the RF domain becomes crucial and requires complex hardware solutions at the first and last layers of the D²NN as demonstrated in Fig. 2. The majority of the literature [55, 56] achieves this conversion using

programmable input layers within the SIM structure, as depicted in Fig. 2(a). Each element of the digital input vector is mapped to the EM response of a corresponding unit element in the initial layer, often through elementary techniques such as amplitude modulation. Subsequently, a beacon signal, usually generated by a single directive antenna, illuminates the back of the first plate to initiate the forward DNN pass.

The final stage, obtaining the D²NN output, requires careful hardware design tailored to the target feature of the EI process. For classification problems, where the output maps to one or more predefined classes, signal receptors equal to the number of classes are placed after the final D²NN layer. The predicted class index (in single class scenarios) corresponds to the receptor registering the highest observed signal strength. For regression problems, obtaining the output is less straightforward. While it is possible to interpret the signal at the receptors as amplitude or phase modulated, achieving the requisite accuracy demands extremely fine grained beamforming capabilities from the SIM, which may be impractical given current D²NN hardware limitations. An example is illustrated in Fig. 2(b), where input receptors with potentially programmable responses are connected through waveguides to an RF chain that combines the absorbed signals to produce the digital output. Specifically during the training phase, once the forward pass is completed and the output is digitized via analog-to-digital converters contained in receive RF chains, the result is compared against the expected target value for each training instance, and the loss function is computed digitally. The backpropagation algorithm is then applied to calculate the necessary changes to the EM responses of each SIM unit element, and this iterative process continues until convergence.

Once the data are successfully converted to the RF regime, D²NNs execute computations at the speed of light, providing a decisive latency advantage over digital DNNs. Perhaps more critical are the benefits concerning power consumption. Fabricated MSs based on near passive circuitry, such as varactors, may operate on power levels as low as a few nanoWatts. This represents a monumental improvement in energy efficiency compared to conventional DNN processors, notably Graphics Processing Units (GPUs), which often consume hundreds of Watts during inference. Furthermore, once the optimal EM responses for the MS unit cells have been determined (typically via simulation), the MSs can be manufactured to be entirely passive. In such scenarios, the only power consuming components of D²NNs are the feeding antenna and the output receptors, all of which can operate under very low power in controlled wireless environments where signal attenuation and multipath effects are minimal. For applications where the input data are intrinsically in the RF domain, such as those related to communications or sensing, the elimination of the power and latency overhead associated with analog-to-digital conversion establishes D²NNs as an ideal candidate for innovative DNN hardware solutions.

3.2 Integration of D²NNs in Wireless Systems

Despite their inherent RF nature, D²NNs have historically been developed primarily as general purpose DNN hardware accelerators, largely isolated from wireless system design. To fully realize their promised advantages in EI applications, the seamless integration of SIM-based computing into the existing wireless communication infrastructure requires substantial research and development. Crucially, the current design paradigm for D²NNs is largely incompatible with existing and prospective wireless stacks.

A major concern revolves around the digital-to-analog conversion of input data. Directly encoding each element of the digital input (e.g., an image pixel) as a pre-mapped EM response of a programmable first SIM layer faces severe limitations for practical deployment: (i) the power consumption of the MS controller required for setting the responses can be considerable, (ii) achieving sufficient precision in programmable MS responses to accurately encode high dimensional input data is technically challenging, and (iii) the physical size of the first MS layer is directly proportional to the dimensionality of the input data.

Furthermore, this current practice fails to leverage the advanced capabilities of contemporary and future wireless systems. Specifically, MIMO systems can utilize transmission across multiple antennas to achieve spatial multiplexing and beamforming gains, thereby introducing new degrees of freedom for feeding input data into the SIM device. From this perspective, standard PHY operations, including source encoding, modulation, and precoding, could be exploited to better integrate D²NNs within MIMO architectures.

Another vital consideration is the impact of the wireless channel on EI performance. Since D²NNs were originally conceived for controlled wireless environments, such as free space, they rely on assumptions of high Signal-to-Noise Ratio (SNR) conditions and negligible, static wireless fading. If D²NNs are to be deployed for inference within wide area wireless networks, dynamic large- and small-scale fading effects can no longer be ignored. In these realistic scenarios, the SIM device assumes a dual functionality: Its learned EM responses must not only execute the inference task, akin to DNN layers, but also continuously adapt to the time varying channel conditions. It is important to emphasize that the effects of the wireless channel should not solely be treated as a source of noise; instead, they can be harnessed as an additional computational resource, aligning with the OAC paradigm [49].

4 Metasurfaces-Integrated Neural Networks

Pondering on the aforementioned limitations of D²NNs in their deployment on realistic wireless systems, it is evident that more advanced DNN architectures are required that incorporate MS-based wave computing practices within an e2e system across the TX and RX devices, as well as the propagation environment. Such designs, dubbed Metasurfaces-Integrated Neural Networks (MINNs) in the following [51], are

designed to also take advantage of wireless MIMO systems and incorporate analog or digital DNN processing at the transceivers. The incorporated D²NN(s) are split at the end devices or reside inside the wireless environment, offering OTA computing with the inclusion of wireless fading [50, 51]. The intention of the MINN system is to offload computation from the transceivers to the environment, allowing for benefits in terms of communication power and computational hardware complexity as well as processing energy. The e2e models presented in this section are designed to accommodate multiple variations in terms of physical devices (including RISs or SIM), placement and capabilities thereof, as well as system objectives.

4.1 System Model

We begin by considering a more comprehensive MIMO system compared to the straightforward one presented in (4) of the previous section in order to account for arbitrary wireless fading and multi-antenna transceiver devices. We further assume the MS device to be located within the environment. Finally, to the intention of providing a unified system and a generic DNN architecture, the system is designed to incorporate either a SIM or RIS device, so the term MS is used, so as to be agnostic of the type of device, and a common notation is adopted for both cases, differentiating between the MS types explicitly wherever needed.

4.1.1 System and Received Signal Models

We analyze the uplink of a point-to-point MIMO communication system, where a TX with N_t antennas transmits data to an N_r -antenna RX over time-indexed frames ($t = 1, 2, \dots$). This communication is enhanced by an MS (either an RIS or SIM), which operates as a standalone node. The MS configuration can be changed at each discrete time step t via an abstract controller [17]. If the MS is a SIM, assume it comprises M thin diffractive layers, each with N_m elements, resulting in a total of $N \triangleq MN_m$ phase-tunable elements. For notational simplicity and to generalize the system model, we also use N to denote the number of tunable elements for an RIS.

Let $\mathbf{H}_D(t) \in \mathbb{C}^{N_r \times N_t}$, $\mathbf{H}_1(t) \in \mathbb{C}^{N_t \times N_m}$, and $\mathbf{H}_2(t) \in \mathbb{C}^{N_r \times N_m}$ be the channel response matrices at time t for the TX-RX, TX-MS, and MS-RX links, respectively. The transmitted signal is $\mathbf{s}(t) \in \mathbb{C}^{N_t \times 1}$, constrained by a power budget $P \triangleq \mathbb{E}[\|\mathbf{s}(t)\|]$. This signal vector encapsulates both the intended, source-coded, and modulated data stream (the number of data symbols $d \leq \min\{N_t, N_r\}$) and potential beamforming weights, without specific assumptions about its generation or symbol distribution.

During each t -th frame transmission, the MS is defined by its controllable *phase configuration* vector $\omega(t) \in \mathbb{C}^{N \times 1}$. The resulting *response configuration*, assuming idealized unit amplitude, is $\phi(t) \triangleq \exp(-j\omega(t))$. The collective effects of the metamaterial responses on the cascaded channel are captured by the matrix $\Phi(t) \in \mathbb{C}^{N_m \times N_m}$, the detailed structure of which is presented in the next subsection.

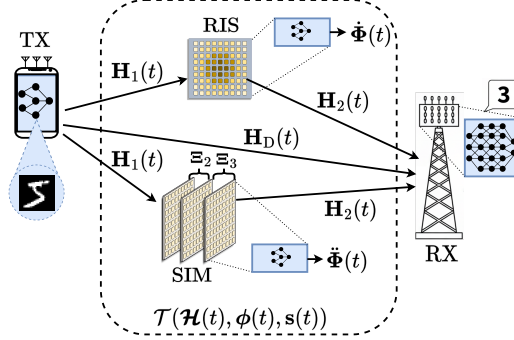


Fig. 3: The MIMO system considered in the MINN framework incorporating either an RIS or a SIM device. The MSs may include a DNN-based controller or a basic processing unit to store or update their fixed configuration.

Throughout this chapter, $\Phi(t)$, $\phi(t)$, and $\omega(t)$ serve as generic notation for both RIS and SIM cases, with device-specific notation introduced only where necessary.

The baseband received signal at the RX antennas is thus given by:

$$\mathbf{y}(t) \triangleq \left(\mathbf{H}_D(t) + \mathbf{H}_2(t)\Phi(t)\mathbf{H}_1^\dagger(t) \right) \mathbf{s}(t) + \tilde{\mathbf{n}} \quad (6)$$

$$\triangleq \mathcal{T}(\mathcal{H}(t), \phi(t), \mathbf{s}(t)), \quad (7)$$

where $\tilde{\mathbf{n}} \in \mathbb{C}^{N_r \times 1}$ is the AWGN at the RX, with independent and identically distributed (i.i.d.) samples drawn from $\mathcal{CN}(0, \sigma^2)$. We utilize the transmission function $\mathcal{T}(\mathcal{H}(t), \phi(t), \mathbf{s}(t))$ as an abstraction, highlighting that the wireless medium is treated as a programmable computation layer. In this formulation, $\mathcal{H}(t) \triangleq \{\mathbf{H}_D(t), \mathbf{H}_1(t), \mathbf{H}_2(t)\}$ denotes the instantaneous CSI. This CSI is assumed to be available to all system nodes. While this availability necessitates a challenging recurring channel estimation phase at each t -th step (see [5] and references therein), this assumption allows us to focus on the training and evaluation of the proposed MINN architecture. Future work could integrate channel estimation into the DNN transceiver modules following Integrated Sensing and Communications (ISAC) principles [57, 58]. Alternatively, channel-agnostic transceiver variations are proposed and evaluated in subsequent sections to assess performance trade-offs when integrating MSs as OTA wave-domain neural network layers. The overall system model is shown in Fig. 3, illustrating the $\mathbf{H}_1(t)$ and $\mathbf{H}_2(t)$ links for both RIS- and SIM-enabled scenarios.

4.1.2 RIS and SIM Models

Starting with the RIS, its phase configuration vector at time t is denoted by $\dot{\omega}(t) \triangleq [\dot{\omega}_1(t), \dots, \dot{\omega}_{N_m}(t)]^\top$, which is equivalent to the generic notation $\omega(t)$ introduced previously. The phase state of its n -th unit element ($n = 1, 2, \dots, N_m$) is $\dot{\omega}_n(t) \in [0, 2\pi]$. The induced response configuration vector is $\dot{\phi}(t) \triangleq \exp(-j\dot{\omega}(t))$, equivalent to $\phi(t)$ in (7). In this case, the response matrix is the diagonal matrix $\dot{\Phi}(t) \triangleq \text{diag}(\dot{\phi}(t)) \in \mathbb{C}^{N_m \times N_m}$, so that $\dot{\Phi}(t)$ is equivalent to $\Phi(t)$ in (6).

For the SIM system model, we assume its M layers ($m = 1, 2, \dots, M$) are closely stacked and parallel, with their shared normal vector perpendicular to the TX-RX link. Under this arrangement, the TX signal first hits the initial layer, undergoes diffraction and controllable phase shifting across the consecutive $M - 1$ layers, and is then finally diffracted toward the RX. Due to the compact spacing, the layer-to-layer propagation is accurately modeled by the Rayleigh-Sommerfeld diffraction equation provided in (4).

In addition to diffraction, each n -th element of the m -th SIM layer introduces a controllable weight, $[\ddot{\phi}_m(t)]_n \triangleq \exp(-j\ddot{\omega}_n^m(t))$, where $\ddot{\omega}_n^m(t) \in [0, 2\pi]$ is the element's phase state. We define $\ddot{\phi}_m(t)$ as the layer m 's response configuration, and $\ddot{\phi}(t) \triangleq [\ddot{\phi}_1^\top(t), \dots, \ddot{\phi}_M^\top(t)]^\top \in \mathbb{C}^{N \times 1}$, which is equivalent to $\phi(t)$, as the overall response configuration. The SIM phase configuration vector is $\ddot{\omega}(t) \triangleq [\ddot{\omega}_1^1(t), \dots, \ddot{\omega}_{N_m}^M(t)]^\top \in \mathbb{C}^{N \times 1}$. The overall SIM response matrix is mathematically expressed through (5) as in the case of D²NNs.

Note that $\Phi(t) \equiv \ddot{\Phi}(t)$ allows (6) to hold for the SIM case. Revisiting the generic notations, $\Phi(t)$ and $\omega(t)$ are now specifically defined as $\Phi(t) \in \{\dot{\Phi}(t), \ddot{\Phi}(t)\}$ and $\omega(t) \in \{\dot{\omega}(t), \ddot{\omega}(t)\}$ for the RIS and SIM respectively. In the rest of the chapter, $\Phi(t)$, $\omega(t)$, and $\phi(t)$ are used when the underlying operations are MS-agnostic, whereas $\dot{\Phi}(t)$, $\ddot{\Phi}(t)$, and their associated vectors are utilized when differentiation between RISs and SIM is required. The notation used to refer to the (generic) MS and each of the RIS and SIM cases is summarized in Table 1.

4.2 DNN Architecture

The general architecture of the MINN framework is consisted of three core modules, as depicted in Fig. 4. The *Encoder* and *Decoder* modules are collocated with the transceivers and act similar to JSCC and GOC modules under the “DNN-splitting” paradigm described earlier. They may be implemented either as fully digital DNNs, running on edge GPUs, or through analog hardware depending on the complexity of the layers and the capabilities of the devices. The channel is treated as an intermediate module that incorporates uncontrollable computations induced by the channel fading and AWGN in combination with controllable computations offered by the MS. The responses of the MS may be treated similar to trainable DNN parameters leading to static configurations, or they may be dynamically controlled through a MS *Controller*.

Table 1: Symbols used to indicate generic MS aspects and the explicit RIS and SIM variations.

Description	Symbol
MS phase configuration vector (generic)	$\omega(t)$
MS response configuration (generic)	$\phi(t)$
Effects of the MS response in the cascaded channel (generic)	$\Phi(t)$
RIS phase state of the n -th element	$\dot{\omega}_n$
RIS phase configuration vector	$\dot{\omega}(t)$
RIS response configuration	$\dot{\phi}(t)$
RIS effects in the cascaded channel	$\dot{\Phi}(t)$
SIM phase state of the n -th unit element of the m -th layer	$\ddot{\omega}_n^m(t)$
SIM phase configuration vector	$\ddot{\omega}(t)$
SIM response configuration vector for the m -th layer	$\ddot{\phi}_m(t)$
SIM response configuration	$\ddot{\phi}(t)$
SIM effects in the cascaded channel	$\ddot{\Phi}(t)$
Output of the penultimate layer of the MS <i>Controller</i>	$\hat{\omega}$
Trainable MS configuration (generic)	$\bar{\omega}$
Trainable MS response (generic)	$\bar{\phi}$
Trainable RIS configuration	$\bar{\omega}_{\text{RIS}}$
Trainable RIS response	$\bar{\phi}_{\text{RIS}}$
Trainable SIM configuration	$\bar{\omega}_{\text{SIM}}$
Trainable SIM response	$\bar{\phi}_{\text{SIM}}$
Trainable SIM's m -th layer effects in the cascaded channel	$\bar{\Phi}_{\text{SIM}}^m$
Trainable SIM's m -th layer response	$\bar{\phi}_{\text{SIM}}^m$

module that leads to reconfigurable instances. The functionality of each module and the training procedure are detailed in the following sections.

4.2.1 Transceiver Modules

As introduced in Section 2.3, EI requires two computational modules, implemented via digital processing hardware, collocated at the transceiver endpoints. To execute the *infer-while-transmitting* methodology, the TX employs an *Encoder* DNN, $f_{\mathbf{w}_e}^e(\cdot)$, which produces the output $\mathbf{s}(t)$, and the RX utilizes a *Decoder* DNN, $f_{\mathbf{w}_d}^d(\cdot)$, which generates the estimate $\hat{\mathbf{o}}(t)$. These modules are responsible for compression, encoding, decoding, error resilience and correction, as well as potential transmit and receive beamforming alongside probabilistic inference. The precise layer architecture of these models is intentionally left open, as the choice depends on several factors: (i) the characteristics of the wireless environment; (ii) the nature of the input and target data; (iii) the transceivers' hardware capabilities; and (iv) the current state-of-the-art. We note that different sub-modules may manage these operations, and typically, for uplink scenarios, $f_{\mathbf{w}_d}^d(\cdot)$ can be implemented with larger DNN structures due to the constant power supply available at base stations. Irrespective of the specific neural network chosen, a fixed post-processing step on the *Encoder*'s output $\mathbf{s}(t)$ is imposed to enforce the TX's power budget as follows:

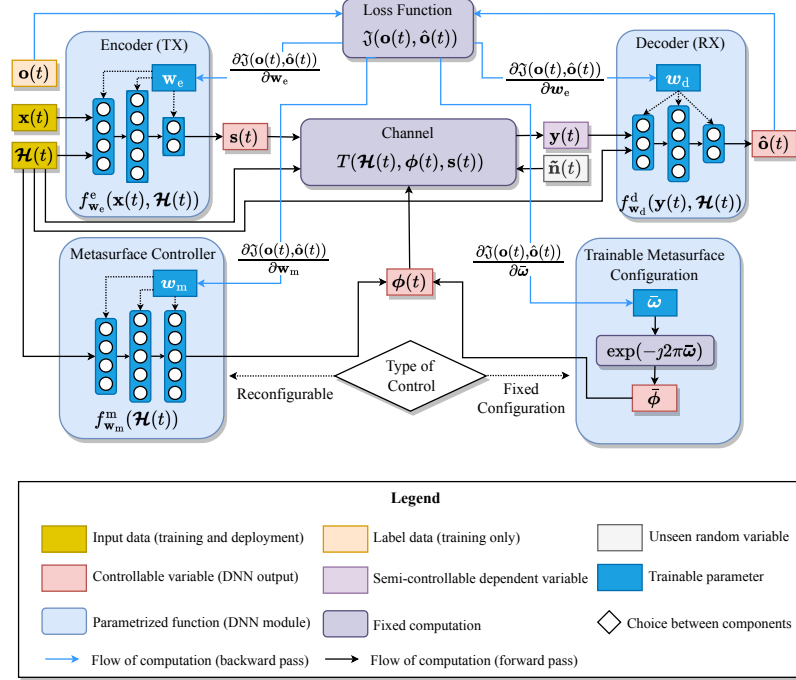


Fig. 4: Block diagram and computation flow of the e2e MINN architecture [51] where the metasurface-parametrizable channel acts as an intermediate DNN component. Both the cases of reconfigurable and static metasurfaces are included, entailing different procedures during the forward and backward passes.

$$s(t) \leftarrow \sqrt{P} \frac{s(t)}{\|s(t)\|}. \quad (8)$$

The concrete input arguments for the *Encoder* and *Decoder* functions lead to two variations, distinguished by the availability of CSI at the endpoints.

Channel-Agnostic Transceivers: In this variation, an instance of the data variable $\mathbf{x}(t)$ is observed by the TX and passed to the *Encoder* to construct the transmitted signal. Concurrently, the *Decoder* DNN observes the received signal and estimates the unseen target variable $\mathbf{o}(t)$:

$$s(t) = f_{\mathbf{w}_e}^e(\mathbf{x}(t)), \quad (9)$$

$$\hat{\mathbf{o}}(t) = f_{\mathbf{w}_d}^d(\mathbf{y}(t)). \quad (10)$$

Since CSI is not utilized by the endpoints, this design resembles source-only coding, even though the *Encoder* may incorporate redundancy, traditionally viewed as channel coding. Both processes must guarantee sufficient inference performance regardless of the current channel conditions, which is a demanding requirement.

Nevertheless, this approach significantly simplifies the system architecture, and we include it in our subsequent investigations.

Channel-Aware Transceivers: Assuming a quasi-static fading channel and a channel estimation procedure preceding data transmission in each t -th frame, the TX and RX modules obtain accurate estimates of the channel response matrices $\mathcal{H}(t)$. Each module may use $\mathcal{H}(t)$ as an additional input, yielding the following *Encoder/Decoder* DNN representations:

$$\mathbf{s}(t) = f_{\mathbf{w}_e}^e(\mathbf{x}(t), \mathcal{H}(t)), \quad (11)$$

$$\hat{\mathbf{o}}(t) = f_{\mathbf{w}_d}^d(\mathbf{y}(t), \mathcal{H}(t)). \quad (12)$$

Equipping the TX/RX modules with CSI enables more resilient transmission schemes that closely resemble JSCC [59]. The primary distinction is that JSCC focuses on reconstructing $\mathbf{x}(t)$, whereas EI aims to approximate $\mathbf{o}(t) = l(\mathbf{x}(t))$. Notice these two problems become equivalent by setting the mapping function $l(\cdot)$ to be the identity function, $\mathbf{o}(t) = \mathbf{x}(t)$, and adopting MSE as the objective function $\mathfrak{J}(\cdot, \cdot)$. Therefore, EI represents a more general problem formulation than communications, which typically concentrate on data reconstruction. For the following, it is assumed that channel estimation is transparent and results in noise-free estimates of $\mathcal{H}(t)$ before every transmission during both training and inference. Accounting for noisy estimates or integrating the estimation process within ISAC paradigms constitutes open research directions.

4.2.2 Control Module for Reconfigurable Metasurfaces

When CSI is available, which is common in many wireless communication contexts, the MS dynamically adjusts its response configuration during each transmission frame to optimize the system's objective [60]. To integrate this dynamic capability into our e2e architecture, the response $\phi(t)$ is modeled as a controllable output of a third digital DNN. Specifically, the MS *Controller* is defined by the following neural network:

$$\phi(t) = f_{\mathbf{w}_m}^m(\mathcal{H}(t)), \quad (13)$$

where the final layer operation enforces $\phi(t) = \exp(-j\hat{\omega})$ with $\hat{\omega}$ representing the output of the penultimate layer, with its elements constrained to the range $[0, 2\pi]$. We maintain the abstract notation $\phi(t)$, acknowledging that the specific output is either $\phi(t)$ or $\ddot{\phi}(t)$ depending on the chosen MS type. This perspective treats the MS as an actively controlled entity capable of adapting to provide favorable wave-domain computation for every channel realization. This fine-grained control over environmental reprogrammability comes at the expense of an additional neural network module and its associated hardware requirements.

By substituting the outputs of the three trained modules from (9), (10), and (13) into the received signal equation (6), we obtain the full e2e inference model $\hat{\mathbf{o}}(t) = f_{\mathbf{w}_r}^r(\mathbf{x}(t), \mathcal{H}(t))$ for both channel knowledge scenarios, as illustrated in Fig.4:

$$\hat{o}(t) = \underbrace{f_{w_d}^d \left(\mathcal{T}(\mathcal{H}(t), f_{w_m}^m(\mathcal{H}(t)), f_{w_e}^e(\mathbf{x}(t))) \right)}_{\text{channel-agnostic transceivers}}, \quad (14a)$$

$$\hat{o}(t) = \underbrace{f_{w_d}^d \left(\mathcal{T}(\mathcal{H}(t), f_{w_m}^m(\mathcal{H}(t)), f_{w_e}^e(\mathbf{x}(t), \mathcal{H}(t))), \mathcal{H}(t) \right)}_{\text{channel-aware transceivers}}. \quad (14b)$$

The entire set of trainable weights for this reconfigurable architecture is defined as $w_r \triangleq \{w_d, w_e, w_m\}$. These weights are jointly optimized using a shared objective function and backpropagation process, detailed in Section 4.3. Note that (14a) deliberately allows the control module to be channel-aware. This implies that the MS possesses sensing capabilities (e.g., [61, 62]) to acquire channel knowledge.

4.2.3 Metasurfaces with Trainable Static Response

An alternative, simplified approach is to directly learn a fixed response configuration for the MS, which we denote by $\bar{\omega}$. Although the training procedure involves optimizing $\bar{\omega}$, the final learned configuration is fixed onto the MS post-training. This results in a constant (static) response configuration $\phi(t) \equiv \bar{\phi} \triangleq \exp(-j\bar{\omega})$ that is maintained over time, regardless of channel conditions or input data. This paradigm treats the effective phase configurations similarly to DNN weights, as they remain fixed after training and perform the same computational operation across varying input instances. The training procedure optimizes the combined weight set $w_s \triangleq \{w_d, w_e, \bar{\omega}\}$.

The e2e static architecture is then expressed as follows:

$$\hat{o}(t) = \underbrace{f_{w_d}^d \left(\mathcal{T}(\mathcal{H}(t), \bar{\phi}, f_{w_e}^e(\mathbf{x}(t))) \right)}_{\text{channel-agnostic transceivers}}, \quad (15a)$$

$$\hat{o}(t) = \underbrace{f_{w_d}^d \left(\mathcal{T}(\mathcal{H}(t), \bar{\phi}, f_{w_e}^e(\mathbf{x}(t), \mathcal{H}(t))), \mathcal{H}(t) \right)}_{\text{channel-aware transceivers}}. \quad (15b)$$

It is important to note that, while reconfigurable MSs provide more granular control over shaping the transmission function $\mathcal{T}(\cdot)$, the inclusion of the MS *Controller* network may hinder the training efficiency of the proposed MINN compared to the static variation. Furthermore, for wireless systems exhibiting limited variability, such as Line-of-Sight (LoS)-dominant environments with fixed transceivers, a static MS configuration may achieve satisfactory performance. The subsequent section ad-

addresses the systemic requirements for all variations presented here, with performance trade-offs explored in the numerical evaluations that follow.

4.3 Training through Backpropagation on Wireless Channels

To train the neural networks at the various wireless communication nodes, we first gather a labeled dataset $\mathcal{D} \triangleq \{(\mathbf{x}_i, \mathbf{o}_i)\}_{i=1}^{|\mathcal{D}|}$ containing $|\mathcal{D}|$ data instances. Additionally, it is assumed access to a set of $|C|$ channel sample estimates $\mathcal{C} \triangleq \{\mathcal{H}(t)\}_{t=1}^{|C|}$ observed at respective coherent time instances, which are not necessarily uniformly spaced. We make the critical assumption that the channel realizations are conditionally independent¹ from the data instances in \mathcal{D} . This conditional independence permits the evaluation of the expectation in the \mathcal{OP}_{EI} objective function via i.i.d. Monte Carlo sampling.

The training process is formulated as a variant of the standard gradient descent method for neural networks, extended to incorporate channel samples. We introduce the generic parameter vector \mathbf{w}_k , where $k \in \{r, s\}$ corresponds to the reconfigurable or static MS selection, respectively. Similar to standard deep learning practices, our e2e MINN architecture can be optimized using SGD over the collected data and channel instances.

The data-channel loss function is expressed as $\mathfrak{J}(\mathbf{o}_i, \hat{\mathbf{o}}_i) = \mathfrak{J}(\mathbf{o}_i, f_{\mathbf{w}_k}^k(\mathbf{x}(t), \mathcal{H}(t)))$, explicitly showing its dependence on the instantaneous wireless channel. Leveraging the conditional independence assumption, the \mathcal{OP}_{EI} objective can be approximated as follows:

$$\mathbb{E}_{\mathcal{H}}[J(\mathbf{w}_k)] \approx \frac{1}{|C||\mathcal{D}|} \sum_{t=1}^{|C|} \sum_{i=1}^{|\mathcal{D}|} \mathfrak{J}(\mathbf{o}_i, f_{\mathbf{w}_k}^k(\mathbf{x}_i, \mathcal{H}(t))). \quad (16)$$

In the online SGD implementation, at each time t , a single data point and channel instance are selected to estimate the gradient, and the parameter vector is updated as:

$$\mathbf{w}_k \leftarrow \mathbf{w}_k - \eta \nabla_{\mathbf{w}_k} \mathfrak{J}(\mathbf{o}(t), f_{\mathbf{w}_k}^k(\mathbf{x}(t), \mathcal{H}(t))), \quad (17)$$

for a chosen learning rate η . The gradient $\nabla_{\mathbf{w}_k} \mathfrak{J}$ is defined based on the MS architecture:

¹ In specific scenarios, the data realizations and channel statistics may be dependent. For instance, in target detection, where \mathbf{x}_i are sensory inputs and \mathbf{o}_i indicates target presence, deep fading may correlate with target blockages. In such cases, channel measurements and data observations must be collected synchronously, necessitating a more intricate EI objective. However, the inference problem might be computationally simplified since CSI provides supplementary information regarding the target value.

Algorithm 1 Training of the Proposed e2e MINN

1: Construct DNN weight vector \mathbf{w}_k as one of the following:
 i) $\mathbf{w}_k = \text{concat}(\mathbf{w}_d, \mathbf{w}_e, \mathbf{w}_m)$. ▷ $\mathbf{w}_k \leftarrow \mathbf{w}_r$
 ii) $\mathbf{w}_k = \text{concat}(\mathbf{w}_d, \mathbf{w}_e, \bar{\omega})$. ▷ $\mathbf{w}_k \leftarrow \mathbf{w}_s$

2: Initialize \mathbf{w}_k randomly.

3: **for** $t = 1, 2, \dots$, until convergence **do**

4: Sample training data instance $(\mathbf{x}(t), \mathbf{o}(t))$ from \mathcal{D} .

5: Sample random channel realization $\mathcal{H}(t)$ from \mathcal{C} .

6: Compute transmit signal $\mathbf{s}(t)$ using one of the following:
 i) $\mathbf{s}(t) = f_{\mathbf{w}_e}^e(\mathbf{x}(t))$. ▷ Eq. (9)
 ii) $\mathbf{s}(t) = f_{\mathbf{w}_e}^e(\mathbf{x}(t), \mathcal{H}(t))$. ▷ Eq. (11)

7: Compute MS response $\phi(t)$ using one of the following:
 i) $\phi(t) = f_{\mathbf{w}_m}^m(\mathcal{H}(t))$. ▷ Eq. (13)
 ii) $\phi(t) = \bar{\phi} = \exp(-j\bar{\omega})$.

8: Transmit $\mathbf{s}(t)$ to receive $\mathbf{y}(t)$:
 $\mathbf{y}(t) = \mathcal{T}(\mathcal{H}(t), \phi(t), \mathbf{s}(t))$. ▷ Eq. (7)

9: Compute output $\hat{\mathbf{o}}(t)$ using one of the following:
 i) $\hat{\mathbf{o}}(t) = f_{\mathbf{w}_d}^d(\mathbf{y}(t))$. ▷ Eq. (10)
 ii) $\hat{\mathbf{o}}(t) = f_{\mathbf{w}_d}^d(\mathbf{y}(t), \mathcal{H}(t))$. ▷ Eq. (12)

10: Update weights \mathbf{w}_k through SGD as:
 $\mathbf{w}_k \leftarrow \mathbf{w}_k - \eta \nabla_{\mathbf{w}_k} \mathfrak{J}(\mathbf{o}(t), f_{\mathbf{w}_k}^k(\mathbf{x}(t), \mathcal{H}(t)))$. ▷ Eq. (17)

11: **end for**

12: **return** \mathbf{w}_k

$$\nabla_{\mathbf{w}_k} \mathfrak{J} = \underbrace{\left[\left[\frac{\partial \mathfrak{J}}{\partial \mathbf{w}_d} \right]^\top, \left[\frac{\partial \mathfrak{J}}{\partial \mathbf{w}_e} \right]^\top, \left[\frac{\partial \mathfrak{J}}{\partial \mathbf{w}_m} \right]^\top \right]^\top}_{\text{reconfigurable metasurface}} \quad (18)$$

$$\nabla_{\mathbf{w}_k} \mathfrak{J} = \underbrace{\left[\left[\frac{\partial \mathfrak{J}}{\partial \mathbf{w}_d} \right]^\top, \left[\frac{\partial \mathfrak{J}}{\partial \mathbf{w}_e} \right]^\top, \left[\frac{\partial \mathfrak{J}}{\partial \bar{\omega}} \right]^\top \right]^\top}_{\text{metasurface with trainable fixed response}} \quad (19)$$

Under the i.i.d. sampling assumption, consecutive gradient evaluations from (17) provide unbiased estimators of the true gradient of (16). Therefore, based on the stochastic approximation framework, repetitive application of this procedure converges to the true expected value with probability 1 up to $O(\eta)$ precision when using a constant step size [63].

The complete training procedure supporting all variations (channel-agnostic-aware transceivers, static/reconfigurable MS controllers, and RIS/SIM structure) is detailed in Algorithm 1. Lines 6–9 implement the MINN architecture as defined in (14) and (15). While more advanced optimization techniques such as batching, momentum, and adaptive rates [64] can be used, they are omitted here for clarity.

The core of the training is the gradient update mechanism in (17). Since (14) and (15) define differentiable operations with respect to \mathbf{w}_s or \mathbf{w}_r , the partial derivatives are computed via automatic differentiation by applying the chain rule to the computational graph. For completeness, we provide the derivations for the partial

derivatives of the various modules, treating the implementation-defined derivatives of the classical neural network components (i.e., $\partial f_{\mathbf{w}_e}^e / \partial \mathbf{w}_e$, $\partial f_{\mathbf{w}_d}^d / \partial \mathbf{w}_d$, $\partial f_{\mathbf{w}_m}^m / \partial \mathbf{w}_m$, and $\partial f_{\mathbf{w}_d}^d / \partial \mathbf{y}(t)$) as known.

4.3.1 Reconfigurable Metasurface (RIS or SIM)

For the reconfigurable MS case, $\hat{\mathbf{o}}$ is given by (14). Applying backpropagation yields the following derivatives:

$$\frac{\partial \mathfrak{J}}{\partial \mathbf{w}_d} = \frac{\partial \mathfrak{J}}{\partial \hat{\mathbf{o}}(t)} \frac{\partial f_{\mathbf{w}_d}^d}{\partial \mathbf{w}_d}, \quad (20)$$

$$\frac{\partial \mathfrak{J}}{\partial \mathbf{w}_m} = \frac{\partial \mathfrak{J}}{\partial \hat{\mathbf{o}}(t)} \frac{\partial f_{\mathbf{w}_d}^d}{\partial \mathbf{y}(t)} \frac{\partial \mathbf{y}(t)}{\partial f_{\mathbf{w}_m}^m} \frac{\partial f_{\mathbf{w}_m}^m}{\partial \mathbf{w}_m}, \quad (21)$$

$$\frac{\partial \mathfrak{J}}{\partial \mathbf{w}_e} = \frac{\partial \mathfrak{J}}{\partial \hat{\mathbf{o}}(t)} \frac{\partial f_{\mathbf{w}_d}^d}{\partial \mathbf{y}(t)} \frac{\partial \mathbf{y}(t)}{\partial f_{\mathbf{w}_e}^e} \frac{\partial f_{\mathbf{w}_e}^e}{\partial \mathbf{w}_e}, \quad (22)$$

where $\partial \mathfrak{J} / \partial \hat{\mathbf{o}}(t)$ is the gradient of the loss function with respect to the network's output (e.g., $-\mathbf{o}(t) / \hat{\mathbf{o}}(t)$ for CE loss). The remaining partial derivatives involving the channel are:

$$\frac{\partial \mathbf{y}(t)}{\partial f_{\mathbf{w}_e}^e} = \mathbf{H}_2(t) \mathbf{\Phi}(t) \mathbf{H}_1^\dagger(t) + \mathbf{H}_D(t), \quad (23)$$

$$\frac{\partial \mathbf{y}(t)}{\partial f_{\mathbf{w}_m}^m} = \frac{\partial \mathbf{y}(t)}{\partial \hat{\mathbf{o}}(t)} = ((\mathbf{s}^\top(t) \mathbf{H}_1^*(t)) \otimes \mathbf{H}_2(t)) \mathbf{D}. \quad (24)$$

4.3.2 RIS with Fixed Configuration

For the fixed-configuration RIS case, $\hat{\mathbf{o}}$ is computed via (15). Let $\bar{\omega}_{\text{RIS}} \in [0, 2\pi)^{N_m}$ and $\bar{\phi}_{\text{RIS}} \triangleq \exp(-J\bar{\omega}_{\text{RIS}})$. Since $\partial \mathfrak{J} / \partial \mathbf{w}_d$ and $\partial \mathfrak{J} / \partial \mathbf{w}_e$ remain the same as in (20) and (22), we focus on the derivative with respect to the trainable configuration $\bar{\omega}$:

$$\frac{\partial \mathfrak{J}}{\partial \bar{\omega}} = \frac{\partial \mathfrak{J}}{\partial \bar{\omega}_{\text{RIS}}} = \frac{\partial \mathfrak{J}}{\partial \hat{\mathbf{o}}(t)} \frac{\partial f_{\mathbf{w}_d}^d}{\partial \mathbf{y}(t)} \frac{\partial \mathbf{y}(t)}{\partial \bar{\phi}_{\text{RIS}}} \frac{\partial \bar{\phi}_{\text{RIS}}}{\partial \bar{\omega}_{\text{RIS}}}, \quad (25)$$

where $\partial \mathbf{y}(t) / \partial \bar{\phi}_{\text{RIS}}$ is computed via (24), and $\partial \bar{\phi}_{\text{RIS}} / \partial \bar{\omega}_{\text{RIS}} = -J \exp(-J\bar{\omega}_{\text{RIS}})$.

4.3.3 Fixed-Configuration SIM

For the fixed configuration SIM case, $\hat{\mathbf{o}}$ is again computed via (15). We use the notations $\bar{\omega}_{\text{SIM}} \in [0, 2\pi)^N$ and $\bar{\phi}_{\text{SIM}} \triangleq \exp(-J\bar{\omega}_{\text{SIM}})$. The gradient is:

$$\frac{\partial \mathfrak{J}}{\partial \bar{\omega}} = \frac{\partial \mathfrak{J}}{\partial \bar{\omega}_{\text{SIM}}} = \frac{\partial \mathfrak{J}}{\partial \hat{\phi}(t)} \frac{\partial f_{w_d}^d}{\partial \mathbf{y}(t)} \frac{\partial \mathbf{y}(t)}{\partial \bar{\phi}_{\text{SIM}}} \frac{\partial \bar{\phi}_{\text{SIM}}}{\partial \bar{\omega}_{\text{SIM}}}, \quad (26)$$

where, $\partial \bar{\phi}_{\text{SIM}} / \partial \bar{\omega}_{\text{SIM}} = -J \exp(-J \bar{\omega}_{\text{SIM}})$. Since $\mathcal{T}(\cdot)$ now incorporates the SIM model from (5), calculating $\partial \mathbf{y}(t) / \partial \bar{\phi}_{\text{SIM}}$ requires further derivation. By denoting the response matrix of the m -th SIM layer as $\bar{\Phi}_{\text{SIM}}^m \triangleq \text{diag}(\bar{\phi}_{\text{SIM}}^m)$, where $\bar{\phi}_{\text{SIM}}^m$ is the trainable response of the m -th layer, we find $\partial \mathbf{y}(t) / \partial \bar{\phi}_{\text{SIM}} = [[\partial \mathbf{y}(t) / \partial \bar{\phi}_{\text{SIM}}^1]^\top, \dots, [\partial \mathbf{y}(t) / \partial \bar{\phi}_{\text{SIM}}^M]^\top]^\top$ with:

$$\frac{\partial \mathbf{y}(t)}{\partial \bar{\phi}_{\text{SIM}}^m} = \begin{cases} (s^\top(t) \mathbf{H}_1^*(t)) \otimes \left(\mathbf{H}_2(t) \prod_{m'=M}^2 \bar{\Phi}_{\text{SIM}}^{m'} \mathbf{\Xi}_{m'} \right) \mathbf{D}, & m = 1 \\ \left(\left(\prod_{m'=m}^2 \mathbf{\Xi}_{m'} \bar{\Phi}_{\text{SIM}}^{m'-1} \right) \mathbf{H}_1^\dagger(t) s(t) \right)^\top & 1 < m \leq M. \\ \otimes (\mathbf{H}_2(t) \prod_{m'=M}^{m+1} \bar{\Phi}_{\text{SIM}}^{m'} \mathbf{\Xi}_{m'}) \mathbf{D}, & \end{cases} \quad (27)$$

In the above, we utilize the identity $\text{vec}(\mathbf{AXB}) = (\mathbf{B}^\top \otimes \mathbf{A})\text{vec}(\mathbf{X})$ and defined the diagonal selection matrix $\mathbf{D} \in [0, 1]^{N_m^2 \times N_m}$ such that, for a vector \mathbf{x} and $\mathbf{X} = \text{diag}(\mathbf{x})$, $\text{vec}(\mathbf{X}) = \mathbf{D}\mathbf{x}$.

5 Image Classification at the Edge

In this section, the performance of the presented MINN framework for the case of multi-class classification on the widely used MNIST data set [65] is demonstrated. This data set contains 60,000 grayscale images of 28×28 pixels, each one depicting a handwritten digit from 0 to 9, and the 10 classes correspond to the numerical value of each depicted digit. We start by considering static fading, i.e., all three matrices \mathbf{H}_D , \mathbf{H}_1 , and \mathbf{H}_2 of \mathcal{H} are sampled using the Saleh-Valenzuela geometric model [66], using 10 scattering points that remain fixed throughout the training and inference scenario. For our MINN system based on a 4×4 MIMO with noise variance $\sigma^2 = -90$ dBm, we incorporate an *Encoder* and a *Decoder* module at the TX and RX, respectively, with three linear layers each and without channel knowledge. The RIS or the SIM have their phase configurations directly trainable without the use of a *Controller* module. Training was conducted for 150 epochs, using the Adam [64] variation of SGD with a learning rate of 10^{-3} and its respective β_1 and β_2 parameters that control the momentum of the updates were set to 0.9 and 0.999, respectively.

As it can be observed from Fig. 5, the combination of increased transmit SNR and greater numbers of elements in the MSs provides substantial benefits in terms of classification accuracy. It is noted that deeper SIM structures are not always more efficient: During the propagation at the SIM layers the signal attenuates with $O(d_{n,n'}^3)$ as it can be observed from (4), which may result to weak signals at the RX, negating the benefits of the additional computation brought by each consecutive SIM in the

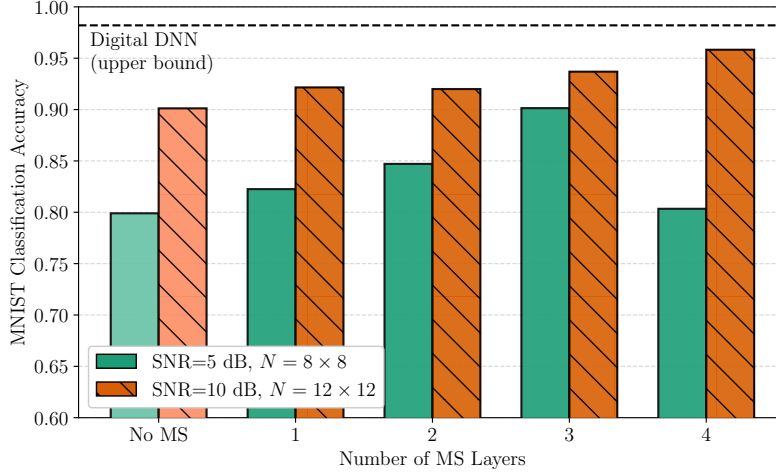


Fig. 5: Mean classification accuracy of MINN on static fading considering RISs and SIM with different numbers of elements and layer, as well as two transmit SNR values.

low SNR regime. On the contrary, under sufficient SNR, deeper SIM architectures can be effective computational models and even approach the performance of the fully digital benchmark. This DNN contains digital layers of the same number and sizes as the *Encoder* and *Decoder* combined and performs inference directly, without accounting for any channel effects, i.e., $\mathcal{T}(\cdot)$ may be thought of as an identity layer.

Proceeding, we investigate the role of the *Controller* module that offers dynamic reconfiguration on the employed MSs instead of relying on static learned responses. To do so, we now adopt dynamic Ricean fading following the model described in detail in [5], so that the CSI changed at every time step t . The Ricean factors (in dB) for the TX-MS, MS-RX, and TX-RX links were respectively set to 13, 7, and 3, providing a case of moderately to strongly dominant line of sight component. To exploit this information, we employ channel-aware *Encoder* and *Decoder* modules as such: In each of these modules, a separate branch of layers receives as inputs the concatenated instantaneous channel matrices $\mathbf{H}_D(t)$, $\mathbf{H}_1(t)$, and $\mathbf{H}_2(t)$ and extracts features to an arbitrary intermediate vector $\mathbf{v}(t)$. The *Encoder* and *Decoder* modules parse their respective inputs ($\mathbf{x}(t)$ and $\mathbf{y}(t)$) through separate branches of three fully connected layers, the outputs of which are concatenated with $\mathbf{v}(t)$ and the resulting intermediate vector is passed through the final two fully connected layers to obtain the respective outputs ($\mathbf{s}(t)$ and $\hat{\mathbf{o}}(t)$). The *Controller* module uses four additional fully connected layers that receive $\mathbf{v}(t)$ as input and output the desired MS configuration $\phi(t)$.

To sufficiently train the MINN variations under dynamic fading on the MNIST data set, the next experiments use 1000 epochs with a transmission power $P = 30$ dBm and $N_r = 32$. Results are averaged over 10 different initializations. The bars

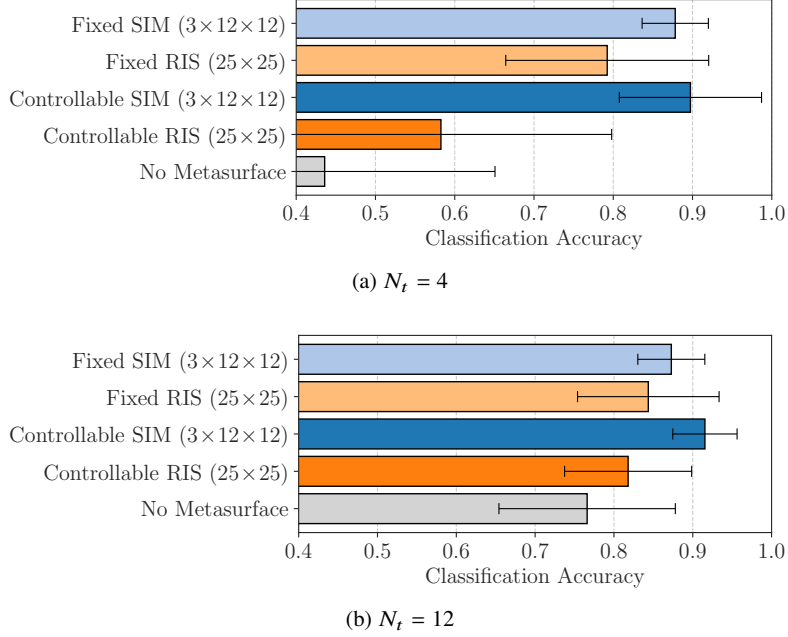


Fig. 6: Mean classification accuracy and standard deviations on the MNIST data set using dynamic Ricean fading under different number of TX antennas and different MINN architectures.

of Fig. 6 depict the mean accuracy under different numbers of TX antennas with their corresponding standard deviations. MINN variations with a Control module are referred to as “Controllable”, while the term “Fixed” corresponds to MINNs that have their MS configurations directly trainable, and therefore remain static during inference regardless of the CSI. It can first be inferred that the use of the Control module offers a slight advantage at the scenario at hand of around 3% accuracy improvement for the SIM cases. The increase in the available link budget when $N_t = 12$ substantially increases the performance of the comparatively less powerful RIS devices and the baseline where EI is performed solely through the *Encoder* and the *Decoder* DNNs without the inclusion of any MS. As expected, the variance across restarts is noticeably reduced. In more dynamic scenarios that incorporate user and/or background scatter mobility, the improvements brought by the *Controller* module are expected to be more pronounced.

Next, the generalization of the MINN framework is investigated over multiple data sets. The Fashion and Kuzushiji MNIST variations have been considered that depict grayscale images of clothing and historical Japanese characters, as well as the CIFAR-10 data set to provide increasing degrees of difficulty. For the two MNIST variations, we have replaced the first three layers of the *Encoder* that parse $\mathbf{x}(t)$ with convolutional layers followed by max-pooling operations, while a deeper con-

Table 2: Estimated computational energy consumption for the *Encoder* device at the TX under the three EI paradigms.

MNIST			
Strategy	$P_{\text{net}}(\text{W})$	$\tau_{\text{inf}}(\text{s})$	$E(\text{mJ/inst.})$
Infer-then-transmit	41.97	8.55	5.98
Transmit-then-infer	44.43	3.27	2.42
Infer-while-transmitting (MINN)	39.61	3.62	2.39
CIFAR-10			
Strategy	$P_{\text{net}}(\text{W})$	$\tau_{\text{inf}}(\text{s})$	$E(\text{mJ/inst.})$
Infer-then-transmit	89.47	10.63	15.85
Transmit-then-infer	43.04	3.68	2.64
Infer-while-transmitting (MINN)	43.82	5.30	3.87

volutional *Encoder* DNN architecture with skip connections has been used for the challenging case of CIFAR-10. The performance across those data sets is given in Fig. 7, where it can be seen that the SIM-based MINN outperforms the RIS variation and the baseline, especially under the case of CIFAR-10.

Since the intention of MINNs is to offload computations onto the wireless channels in order to simplify transceiver hardware, we further elaborate on the energy consumption benefits of the presented methodologies. We compare against the two other methodologies presented in Section 2.3. In the “infer-then-transmit” paradigm, the classification is solved at the TX using the “Digital DNN” benchmark discussed earlier for MNIST as well as the *Encoder* architecture for CIFAR-10 with three more layers added for final classification. A perfect transmission of the result is assumed, since it requires mere $\log_2(10) \approx 3.32$ bits. For the “transmit-then-infer” case, we compress the input images using a compression scheme based on pre-trained Auto-Encoders (AEs), and we transmit the encoded representations using Phase Shift Keying (PSK) modulation and capacity achieving MIMO precoding and combining. The “Digital DNN” is thus placed at the RX and classifies the reconstructed images, achieving up to 80% accuracy due to the limited transmission budget. The power required for the computation of the TX processing P_{net} is measured experimentally in the workstation used to run the experiments for each case, while the latency τ_{inf} associated with performing inference over the test set is also recorded. The consumed energy per data instance is therefore calculated as $E = P_{\text{net}}/\tau_{\text{inf}}$. Those numbers are presented in Table 2. It can be seen that the MINN system architecture consumes energy comparable to the “transmit-then-infer” method which contains only the minimum processing for transmission, while it maintains an around 10% performance improvement in terms of classification accuracy, motivating the OTA methodology developed in this chapter.

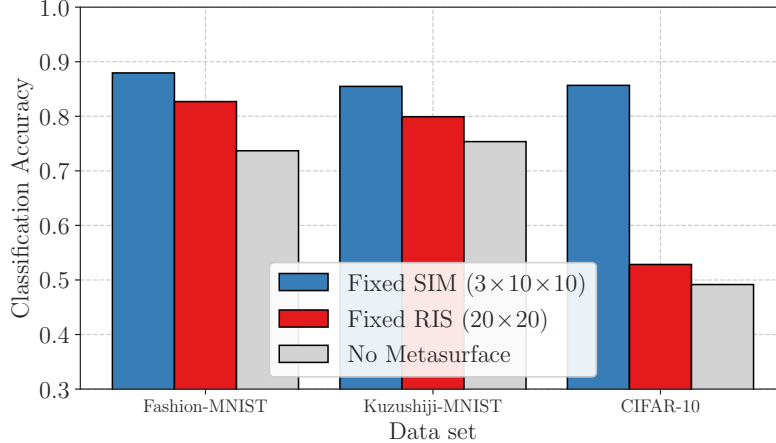


Fig. 7: Mean accuracy with different MINN variations and the No-MS baseline, considering different data sets, fixed configuration MSs, and channel-agnostic transceivers.

6 Transmission Power Control

Having showed that MINNs may offer accuracy approaching that of fully digital DNNs with reduced computational power requirements at the TX side, it raises the question whether power savings for data transmission may also be achievable. As illustrated in Fig. 5, higher transmission power indeed offers better inference accuracy. However, the previous MINN architectures were trained in fixed, high-SNR conditions, which did not incentivize training to generalize to low-SNR regimes.

To specifically treat this limitation, a MINN variation is developed next, where the e2e system learns to control the transmission power dynamically during training. This is particularly designed for dynamic fading scenarios where one of the endpoints (typically, the RX in downlink communications) is mobile, and therefore the required power level depends on the dynamic fading conditions of the instantaneous links. In doing so, let us consider a modified version of the EI problem [67]. Based on a collected data set \mathcal{D} and corresponding channel realizations \mathcal{H} , the MINN is seen as a mapping function $\{\hat{\mathbf{o}}(t), P(t)\} \triangleq f_{\bar{\mathbf{w}}}(\mathbf{x}(t), \mathcal{H}(t))$, parametrized by a weight vector $\bar{\mathbf{w}}$, that outputs an estimate $\hat{\mathbf{o}}(t)$ for $\mathbf{o}(t)$ as well as the TX power $P(t)$. We thereby propose the following problem formulation for the design of $\bar{\mathbf{w}}$:

$$\min_{\bar{\mathbf{w}}} \mathcal{L}(\bar{\mathbf{w}}) \triangleq \mathbb{E}_{\mathcal{H}} \left[\frac{1}{|\mathcal{D}|} \sum_{i=1}^{|\mathcal{D}|} \mathfrak{J}_{\text{CE}}(\hat{\mathbf{o}}(i), \mathbf{o}(i)) \right], \quad (28a)$$

$$\text{s.t. } \{\hat{\mathbf{o}}(i), P(i)\} = f_{\bar{\mathbf{w}}}(\mathbf{x}(i), \mathcal{H}(i)), \quad (28b)$$

$$\mathbb{E}_{\mathcal{H}}[P(i)] \leq P_{\max} \quad \forall i = 1, \dots, |\mathcal{D}|, \quad (28c)$$

where $\mathbb{E}_{\mathcal{H}}[\cdot]$ represents expectation over the channels, which is computed empirically as in (16). Once problem (28) is solved, $f_{\bar{\mathbf{w}}}(\cdot)$ may be used to infer the target values for previously unseen input data that follow the same distribution as those in \mathcal{D} .

For our MINN architecture, we use the channel agnostic *Encoder* and *Decoder* modules $\bar{s}(t) = f_{\mathbf{w}_e}^e(\mathbf{x}(t))$ and $\hat{\mathbf{o}}(t) = f_{\mathbf{w}_d}^d(\mathbf{y}(t))$ from (9) and (10), respectively, as before. We incorporate a new, *Power Control* module, $P(t) = f_{\mathbf{w}_p}^p(\mathbf{p}(t))$, which receives the current position of the RX, $\mathbf{p}(t) = [x(t), y(t)]$, and outputs the power value to be used for $\mathbf{x}(i)$'s transmission. Note that the input data are not used by this module allowing it to focus on beneficial power control strategies based solely on $\mathbf{p}(t)$'s.

The *Channel* module using a SIM, $\mathbf{y}(t) = f_{\bar{\omega}}^c(\mathbf{x}(t), P(t), \mathcal{H}(t))$, implements the OTA propagation as in (6) with $\bar{s}(t) = P(t)s(t)$ incorporating the dynamic power control. Recall that the channel is parametrized by the vector $\bar{\omega} = [\bar{\omega}_1^\top, \dots, \bar{\omega}_M^\top]^\top \in [0, 2\pi]^N$ containing all SIM elements' tunable responses, which are treated equivalently to trainable DNN parameters. Aggregating the parameters of all subsequent modules into the vector $\bar{\mathbf{w}} \triangleq [\mathbf{w}_t^\top, \mathbf{w}_p^\top, \bar{\omega}^\top, \mathbf{w}_r^\top]^\top$ results in the proposed MINN:

$$\hat{\mathbf{o}}(t) = f_{\mathbf{w}_r}^r(f_{\bar{\omega}}^c(f_{\mathbf{w}_t}^t(\mathbf{x}(t)), f_{\mathbf{w}_p}^p(\mathbf{p}(t)), \mathcal{H}(t))), \quad (29)$$

which is optimized to address a relaxed variation of problem (28). Specifically, by integrating the constraint (28c) into the objective of (28a), we obtain the following design formulation for $\bar{\mathbf{w}}$:

$$\min_{\bar{\mathbf{w}}} \hat{\mathcal{L}}(\bar{\mathbf{w}}) \triangleq \mathbb{E}_{\mathcal{H}} \left[\sum_{i=1}^{|\mathcal{D}|} \mathfrak{J}_{\text{CE}}(\hat{\mathbf{o}}(i), \mathbf{o}(i)) + \gamma P(i) \right] \quad (30a)$$

$$\text{s.t. } \{\hat{\mathbf{o}}(i), P(i)\} = f_{\bar{\mathbf{w}}}(\mathbf{x}(i), \mathcal{H}(i)), \quad i = 1, \dots, |\mathcal{D}|, \quad (30b)$$

$$[\bar{\omega}_m]_n \in [0, 2\pi], \quad \forall n = 1, \dots, N_m, \quad m = 1, \dots, M, \quad (30c)$$

where γ represents a Lagrange multiplier, empirically tuned to satisfy the P_{\max} constraint. To ensure that all phase shifts reside in the $[0, 2\pi]$ range (satisfying (30c)), the operation $\bar{\omega} \leftarrow \pi(\tan^{-1}(\bar{\omega}) + 1)$ is applied to them. Throughout the remainder, $(\mathbf{x}(t), \mathbf{o}(t))$ and $\mathcal{H}(t)$ are assumed to be statistically independent, implying the data has no correlation with the wireless environment. This assumption guarantees that independently sampled random pairs of $(\mathbf{x}(t), \mathbf{o}(t))$ and $\mathcal{H}(t)$ yield unbiased estimators for the expectation of $\hat{\mathcal{L}}(\bar{\mathbf{w}})$ [68]. Consequently, we employ SGD with backpropagation [31] on (30a) to determine approximately optimal values for $\bar{\mathbf{w}}$. The chain rule derivation for the partial derivatives of the DNN module weights follows

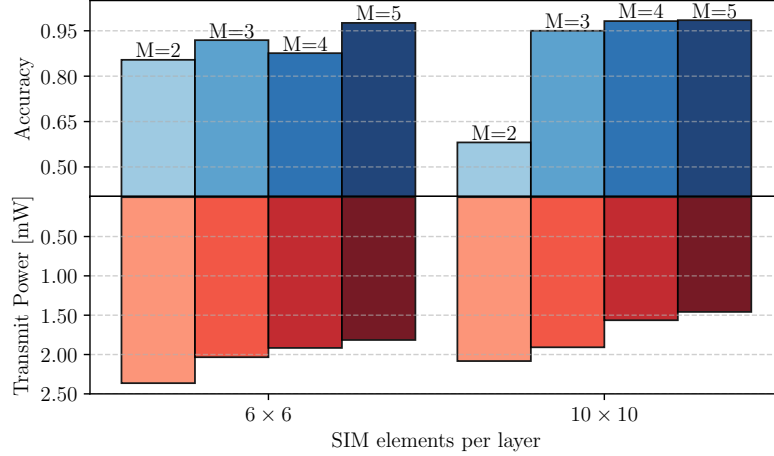


Fig. 8: Achieved MNIST classification accuracy and corresponding transmission power during inference for different numbers of SIM layers and different numbers of elements per layer considering MINN with integrated power control. The accuracy-power tradeoff parameter γ is set to 10^{-2} for this case.

the derivations of Section 4.3. Crucially, the digital DNN modules do not require channel matrix information during the forward pass (i.e., during deployment), as $f_{\omega}^c(\cdot)$ is implemented OTA. However, training necessitates an analytical model for $f_{\omega}^c(\cdot)$ and knowledge of $\mathcal{H}(t)$ to facilitate gradient backpropagation to the *Encoder* and *Power Control* modules.

To numerically evaluate the performance of the MINN with integrated power control we continue the MNIST classification scenarios, considering 16×8 MIMO channels from the Saleh-Valenzuela model [66] with 20 fixed scatterers, while we randomly place the RX within the wireless environment at every time step to create dynamic fading. We allow the training to take place over 200 epochs under the following procedure: During the first 30 epochs, the *Power Control* module $f_{\mathbf{w}_p}^p(\mathbf{p}(t))$ does not partake in the process. Instead $P(t)$ is set to 30 dBm and both the forward and backward passes involve the *Encoder*, *Decoder*, and *Channel* modules, following the typical MINN description presented in the previous sections. After the 30th epoch, $f_{\mathbf{w}_p}^p(\mathbf{p}(t))$ is inserted into the training loop and \mathbf{w}_p is updated as part of $\bar{\mathbf{w}}$. The motivation for this is that DNNs perform most of their learning during the first few iterations, where the objective function decreases rapidly. It is therefore especially important for the highest quality of data to be present at this earlier stage. In fact, introducing the *Power Control* module's trainable parameters at a later stage during training can be seen as a form of transfer learning and domain adaptation [69], where the network learns to adapt to different conditions, imposed by the penalty term of the objective function.

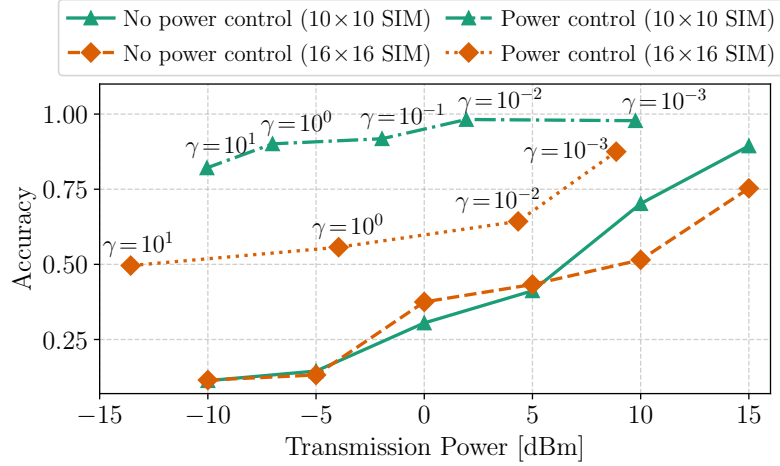


Fig. 9: Achieved MNIST classification accuracy for MINNs of 4 SIM layers with integrated power control with different tradeoff γ values compared to MINNs trained with fixed transmission power levels.

Considering different numbers of layers and elements per layers, classification accuracy results are depicted in Fig. 8, where each case is accompanied by the minimum power attained by the MINN while achieving the reported accuracy. It can be inferred that deeper architectures provide improvements in terms of accuracy, but more crucially, in terms of energy efficiency. Moreover, the effects of the Lagrange multiplier are investigated in Fig. 9. In the figure, MINNs with integrated power control are compared against counterparts trained with fixed transmission powers during training to illustrate the benefits of dynamic power manipulation. As it can be seen, under the same power budgets, MINNs with integrated power control achieve considerably larger accuracy results, especially under very low SNR. In fact, for the case of the 10×10 SIM, the MINN without power control achieves comparable accuracy only at the cost of 25 dB higher power consumption.

7 Open Challenges

Despite the growing maturity of MS technology [17, 70], D²NN prototypes, and relevant algorithmic approaches, MINNs remain in their infancy. The primary limitations of this technology highlight several critical avenues for future research, as outlined below.

Nonlinearity: Existing MS designs and models rely principally on linear computations. Consequently, the *Channelmodule* acts as a *single linear* layer, regardless of how many SIM layers are utilized. These basic linear layers offer only limited approx-

imation capabilities. To realize truly deep OTA architectures, nonlinear activation functions must be integrated into the layer-to-layer metasurface propagation. This could be achieved through advanced metamaterial designs capable of exhibiting nonlinear responses in the RF domain. Emerging metamaterials or passive/near-passive RF circuits offer promising prospects in this regard. Notably, these nonlinear responses do not necessarily require controllability, as activation functions in DNNs are typically fixed [71].

Advanced DNN architectures: Beyond achieving greater depth, state-of-the-art models utilize sophisticated layer architectures that surpass the capabilities of the fully-connected feedforward propagation found in D²NNs. While recent efforts have successfully implemented convolutional layers by leveraging wideband characteristics [72], the implementation of deep convolutional neural networks, or even more complex recurrent and attention-based architectures remains, a formidable challenge.

Theoretical guarantees: Regardless of the specific MS design or layer architecture selected, establishing the universal approximation properties when accounting for the operations induced by the channel is a difficult task. For Single hidden Layer Feedforward Networks (SLFNs) where channel fading coefficients can play the role of random weight parameters in the hidden layer, it can be shown [71] that this simplified MINN architecture exhibits the characteristics of universal approximation. This theoretical result holds by casting the MINN under the Extreme Learning Machine (ELM) framework under the following conditions: (i) static Rayleigh fading, (ii) arbitrarily large, yet finite, N_r , and (iii) nonlinear activation function at the RX, which may be implemented using analog RF components. Further theoretical advancements are required to extend the guarantees associated with random weights to deeper structures and dynamic fading environments. Complementary analytical insights could also guide best practices for regularization, initialization, and hyper-parameter selection, leading to more stable training behavior.

Exploitation of temporal and frequency degrees of freedom: To date, D²NNs and MINNs have primarily exploited spatial degrees of freedom via multiplexing across multiple antenna/MS elements. However, temporal and frequency degrees of freedom remain underexplored [56]. By leveraging wideband and frequency-selective MS responses [73], the duality between time and frequency domains can be effectively exploited. In this context, reconfigurable MSs could enable feature extraction across multiple transmissions. Furthermore, equipping the system with temporal memory beyond linear time-invariant limits offers a potential pathway for implementing recurrent layers.

OTA training: Training for MINN and D²NNs is typically assumed to occur in simulation, where gradient updates are computed digitally before the resulting responses are forwarded to the MSs. However, more advanced MS designs may eventually allow for the objective function and corresponding gradients to be calculated OTA. This would enable the backward pass to be performed in the wave domain by reconfiguring MS responses according to impinging error signals.

8 Conclusions

GOOC are gaining momentum in the emerging data-driven networks as they reduce the amount of data transmitted and the associated computations. Performing EI, in particular, involves DNN-based *Encoder* and *Decoder* modules at the TX and RX devices, respectively. To this end, the whole system can be treated as a single DNN and be trained through backpropagation over the channel that induces fading effects. By employing various types of MSs onto the wireless environment environment, the propagation of RF signals can be controlled to perform operations similar to linear layers of DNN OTA. The basic principle relies on SIM-based computational units that implement D²NNs for wave-domain ML. SIM or RIS devices can further be positioned inside the wireless channel so that they shape the resulting dynamic fading to perform desirable ML computations. Consequently, the *Encoder*, MS-parametrized *Channel*, and *Decoder* modules now comprise an e2e trainable MINN architecture with OTA computation capabilities that offload part of the processing onto the channel, therefore reducing the overall computational power consumption. Different variations may be supported, including channel-aware or channel-agnostic transceivers and MSs with fixed or dynamically reconfigurable responses, that achieve performance on par with their fully digital counterparts. By further incorporating dynamic power control during training, MINN architectures may learn to reduce the transmission power needed during inference. Once important challenges related to nonlinear MS responses and advanced ML operations are overcome, MINN are foreseen to constitute a key pillar of energy-efficient intelligent designs for autonomous network applications under communications and sensing.

References

1. N. A. Mohammed, A. M. Mansoor, and R. B. Ahmad, “Mission-critical machine-type communication: An overview and perspectives towards 5G,” *IEEE Access*, vol. 7, pp. 127 198–127 216, 2019.
2. B. Aazhang, P. Ahokangas, H. Alves, M.-S. Alouini, J. Beek, H. Benn, M. Bennis, J. Belfiore, E. Strinati, F. Chen, K. Chang, F. Clazzer, S. Dizit, D. Kwon, M. Giordiani, W. Haselmayr, J. Haapola, E. Hardouin, E. Harjula, and P. Zhu, “Key drivers and research challenges for 6G ubiquitous wireless intelligence (white paper),” 6G Flagship, University of Oulu, Oulu, Finland, Tech. Rep., sep 2019.
3. K. B. Letaief, Y. Shi, J. Lu, and J. Lu, “Edge artificial intelligence for 6G: Vision, enabling technologies, and applications,” *IEEE J. Sel. Areas Commun.*, vol. 40, no. 1, pp. 5–36, 2022.
4. A. Li, S. Wu, S. Meng, and Q. Zhang, “Towards goal-oriented semantic communications: New metrics, open challenges, and future research directions,” *arXiv preprint:2304.00848*, 2023.
5. G. C. Alexandropoulos, K. Stylianopoulos, C. Huang, C. Yuen, M. Bennis, and M. Debbah, “Pervasive machine learning for smart radio environments enabled by reconfigurable intelligent surfaces,” *Proc. IEEE*, vol. 110, no. 9, pp. 1494–1525, Sep. 2022.
6. G. C. Alexandropoulos, S. Samarakoon, M. Bennis, and M. Debbah, “Phase configuration learning in wireless networks with multiple reconfigurable intelligent surfaces,” in *Proc. IEEE Global Commun. Conf.*, Taipei, Taiwan, Dec. 2020.

7. C. Huang, Z. Yang, G. C. Alexandropoulos, K. Xiong, L. Wei, C. Yuen, Z. Zhang, and M. Debbah, "Multi-hop RIS-empowered terahertz communications: A DRL-based hybrid beamforming design," *IEEE Jel. Sel. Areas Commun.*, vol. 39, no. 6, pp. 1663–1677, 2021.
8. G. Stamatelis, K. Stylianopoulos, and G. C. Alexandropoulos, "Evolving multi-branch attention convolutional neural networks for online RIS configuration," *IEEE Trans. Cogn. Commun. Netw.*, early access, 2025.
9. K. Stylianopoulos and G. C. Alexandropoulos, "Online RIS configuration learning for arbitrary large numbers of 1-bit phase resolution elements," in *Proc. IEEE Int. Workshop Signal Process. Adv. Wireless Commun. (SPAWC)*, Oulu, Finland, 04–06 Jul 2022.
10. J. Deng, G. Li, Q. Zheng, Z. Wen, C. Pan, Q. Wang, G. Liu, G. Li, H. Cai, Y. Liang, P. Zhao, and L. Yu, "6G native AI architecture and technologies white paper," China Mobile Research Institute (CMRI), Tech. Rep., 2022.
11. K. Stylianopoulos, M. Bayraktar, N. González-Prelcic, and G. C. Alexandropoulos, "Autoregressive attention neural networks for non-line-of-sight user tracking with dynamic metasurface antennas," in *Proc. IEEE Int. Workshop Comput. Adv. Multi-Sensor Adaptive Process. (CAMSAP)*, 2023, pp. 391–395.
12. G. C. Alexandropoulos, D.-T. Phan-Huy, K. D. Katsanos, M. Crozzoli, H. Wymeersch, P. Popovski, P. Ratajczak, Y. Bénédic, M.-H. Hamon, S. H. Gonzalez *et al.*, "RIS-enabled smart wireless environments: Deployment scenarios, network architecture, bandwidth and area of influence," *EURASIP J. Wireless Commun. and Netw.*, vol. 2023, no. 1, pp. 1–38, Oct. 2023.
13. M. Di Renzo, M. Debbah, D.-T. Phan-Huy, A. Zappone, M.-S. Alouini, C. Yuen, V. Sciancalepore, G. C. Alexandropoulos, J. Hoydis, H. Gacanin, J. de Rosny, A. Bounceu, G. Leroosey, and M. Fink, "Smart radio environments empowered by reconfigurable AI meta-surfaces: An idea whose time has come," *EURASIP J. Wireless Commun. Net.*, vol. 2019, no. 1, pp. 1–20, May 2019.
14. B. Yang, X. Cao, J. Xu, C. Huang, G. C. Alexandropoulos, L. Dai, M. Debbah, H. V. Poor, and C. Yuen, "Reconfigurable intelligent computational surfaces: When wave propagation control meets computing," *IEEE Wireless Commun.*, vol. 30, no. 3, pp. 120–128, 2023.
15. G. C. Alexandropoulos, N. Shlezinger, and P. del Hougne, "Reconfigurable intelligent surfaces for rich scattering wireless communications: Recent experiments, challenges, and opportunities," *IEEE Commun. Mag.*, vol. 59, no. 6, pp. 28–34, 2021.
16. C. Huang, A. Zappone, G. C. Alexandropoulos, M. Debbah, and C. Yuen, "Reconfigurable intelligent surfaces for energy efficiency in wireless communication," *IEEE Trans. Wireless Commun.*, vol. 18, no. 8, pp. 4157–4170, Aug. 2019.
17. E. Basar, G. C. Alexandropoulos, Y. Liu, Q. Wu, S. Jin, C. Yuen, O. A. Dobre, and R. Schober, "Reconfigurable intelligent surfaces for 6G: Emerging hardware architectures, applications, and open challenges," *IEEE Veh. Technol. Mag.*, vol. 19, no. 3, pp. 27–47, 2024.
18. J. An, C. Xu, D. W. K. Ng, G. C. Alexandropoulos, C. Huang, C. Yuen, and L. Hanzo, "Stacked intelligent metasurfaces for efficient holographic MIMO communications in 6G," *IEEE J. Sel. Areas Commun.*, vol. 41, no. 8, pp. 2380–2396, 2023.
19. K. R. R. Ranasinghe, I. A. M. Sandoval, G. T. F. de Abreu, and G. C. Alexandropoulos, "Parametrized stacked intelligent metasurfaces for bistatic integrated sensing and communications," in *Proc. IEEE Asilomar Signals, Syst. Comput. Conf.*, Pacific Grove, USA, 6–29 Oct 2025, pp. 1–5.
20. C. Huang, G. C. Alexandropoulos, C. Yuen, and M. Debbah, "Indoor signal focusing with deep learning designed reconfigurable intelligent surfaces," in *Proc. IEEE Int. Workshop Signal Process. Adv. Wireless Commun.*, Cannes, France, 2–5 July 2019, pp. 1–6.
21. C. Huang, S. Hu, G. C. Alexandropoulos, A. Zappone, C. Yuen, R. Zhang, M. Di Renzo, and M. Debbah, "Holographic MIMO surfaces for 6G wireless networks: Opportunities, challenges, and trends," *IEEE Wireless Commun.*, vol. 27, no. 5, pp. 118–125, Oct. 2020.
22. Z. R. Omam, H. Taghvaei, A. Araghi, M. Garcia-Fernandez, G. Alvarez-Narciandi, G. C. Alexandropoulos, O. Yurduseven, and M. Khalily, "Holographic metasurfaces enabling wave computing for 6G: Status overview, challenges, and future research trends," *arXiv preprint:2501.05173*, 2025.

23. V. Jamali, G. C. Alexandropoulos, R. Schober, and H. V. Poor, "Low-to-zero-overhead IRS re-configuration: Decoupling illumination and channel estimation," *IEEE Commun. Lett.*, vol. 26, no. 4, pp. 932–936, 2022.
24. A. L. Moustakas, G. C. Alexandropoulos, and M. Debbah, "Reconfigurable intelligent surfaces and capacity optimization: A large system analysis," *IEEE Transa. Wireless Commun.*, vol. 22, no. 12, pp. 8736–8750, 2023.
25. K. Stylianopoulos, P. Gavriilidis, and G. C. Alexandropoulos, "Asymptotically optimal closed-form phase configuration of 1-bit RISs via sign alignment," in *Proc. IEEE Int. Workshop Signal Process. Adv. Wireless Commun. (SPAWC)*, Lucca, Italy, 10-13 Sept 2024, pp. 746–750.
26. P. Gavriilidis, K. Stylianopoulos, and G. C. Alexandropoulos, "MIMO communications with 1-bit RIS: Asymptotic analysis and over-the-air channel diagonalization," in *Proc. IEEE Asilomar Signals, Syst. Comput. Conf.*, Pacific Grove, USA, 26–29 October 2025, pp. 1–5.
27. P. Gavriilidis and G. C. Alexandropoulos, "Near-field beam tracking with extremely large dynamic metasurface antennas," *IEEE Trans. Wireless Commun.*, vol. 24, no. 7, pp. 6257–6272, 2025.
28. D. J. C. MacKay, *Information Theory, Inference, and Learning Algorithms*. Cambridge, U.K.: Cambridge University Press, 2003.
29. I. Goodfellow, Y. Bengio, and A. Courville, *Deep Learning*. MIT Press, 2016, <http://www.deeplearningbook.org>.
30. G. Cybenko, "Approximation by superpositions of a sigmoidal function," *Math. Control Signals Syst.*, vol. 2, no. 4, pp. 303–314, 1989.
31. D. E. Rumelhart, G. E. Hinton, and R. J. Williams, "Learning representations by back-propagating errors," *Nature*, vol. 323, no. 6088, pp. 533–536, Oct 1986.
32. Y. LeCun, L. D. Jackel, B. Boser, J. S. Denker, D. Henderson, H. P. Graf, and D. Judd, "Backpropagation applied to handwritten zip code recognition," *Neural Comput.*, vol. 1, pp. 541–551, 1989.
33. F. Binucci, M. Merluzzi, P. Banelli, E. Calvanese Strinati, and P. Di Lorenzo, "Enabling edge artificial intelligence via goal-oriented deep neural network splitting," in *Proc. Int. Symp. Wireless Commun. Syst.*, Rio de Janeiro, Brazil, 2024.
34. D. P. Kingma and M. Welling, "Auto-encoding variational Bayes," in *Proc. Int. Conf. Learn. Represent.*, Banff, AB, Canada, 2014.
35. O. Ronneberger, P. Fischer, and T. Brox, "U-Net: Convolutional networks for biomedical image segmentation," in *Proc. Med. Image Comput. Comput. Assist. Interv.*, Munich, Germany, 2015.
36. S. Dörner, S. Cammerer, J. Hoydis, and S. ten Brink, "Deep learning based communication over the air," *IEEE J. Sel. Top. Signal Process.*, vol. 12, no. 1, pp. 132–143, 2018.
37. E. Bourtsoulatze, D. B. Kurka, and D. Gündüz, "Deep joint source-channel coding for wireless image transmission," in *Proc. Int. Conf. Acoust. Speech Signal Process.*, Brighton, UK, 2019.
38. C. E. Shannon, "A mathematical theory of communication," *Bell Syst. Tech. J.*, vol. 27, pp. 379–423, 1948.
39. D. Gündüz, Z. Qin, I. E. Aguerri, H. S. Dhillon, Z. Yang, A. Yener, K. K. Wong, and C.-B. Chae, "Beyond transmitting bits: Context, semantics, and task-oriented communications," *IEEE J. Select. Areas Commun.*, vol. 41, no. 1, pp. 5–41, 2023.
40. H. Xie, Z. Qin, G. Y. Li, and B.-H. Juang, "Deep learning enabled semantic communication systems," *IEEE Trans. Signal Process.*, vol. 69, pp. 2663–2675, 2021.
41. M. Jankowski, D. Gündüz, and K. Mikolajczyk, "Wireless image retrieval at the edge," *IEEE J. Sel. Areas Commun.*, vol. 39, no. 1, pp. 89–100, 2021.
42. F. Pezone, S. Barbarossa, and P. Di Lorenzo, "Goal-oriented communication for edge learning based on the information bottleneck," in *IEEE Int. Conf. Acoust. Speech Signal Process. (ICASSP)*, Singapore, Singapore, 23-27 May 2022, pp. 8832–8836.
43. N. Hello, M. Merluzzi, E. Calvanese Strinati, and L. Sanguinetti, "Optimizing RIS impairments through semantic communication," *arXiv preprint:410.08155*, 2024.
44. P. A. Stavrou and M. Kountouris, "A rate distortion approach to goal-oriented communication," in *Proc. IEEE Int. Symp. Inf. Theory*, Espoo, Finland, 2022.

45. N. Srivastava, G. Hinton, A. Krizhevsky, I. Sutskever, and R. Salakhutdinov, “Dropout: A simple way to prevent neural networks from overfitting,” *J. Mach. Learn. Res.*, vol. 15, no. 1, p. 1929–1958, 2014.
46. C. Gulcehre, M. Moczulski, M. Denil, and Y. Bengio, “Noisy activation functions,” in *Proc. Int. Conf. Mach. Learn.*, vol. 48, New York, USA, 2016.
47. D. P. Kingma, T. Salimans, and M. Welling, “Variational dropout and the local reparameterization trick,” in *Proc. Adv. Neural Inf. Process. Syst.*, vol. 28, Montreal, Canada, 2015.
48. Y. Gal and Z. Ghahramani, “Dropout as a Bayesian approximation: Representing model uncertainty in deep learning,” in *Proc. Int. Conf. Mach. Learn.*, vol. 48, New York, USA, 2016.
49. Z. Wang, Y. Zhao, Y. Zhou, Y. Shi, C. Jiang, and K. B. Letaief, “Over-the-air computation for 6G: Foundations, technologies, and applications,” *IEEE Internet Things J.*, vol. 11, no. 14, pp. 24 634–24 658, 2024.
50. G. Huang, J. An, Z. Yang, L. Gan, M. Bennis, and M. Debbah, “Stacked intelligent metasurfaces for task-oriented semantic communications,” *arXiv preprint:2407.15053*, 2024.
51. K. Stylianopoulos, P. Di Lorenzo, and G. C. Alexandropoulos, “Over-the-air edge inference via metasurfaces-integrated artificial neural networks,” *arXiv preprint:2504.00233*, 2025.
52. X. Lin, Y. Rivenson, N. T. Yardimci, M. Veli, Y. Luo, M. Jarrahi, and A. Ozcan, “All-optical machine learning using diffractive deep neural networks,” *Science*, vol. 361, no. 6406, pp. 1004–1008, 2018.
53. K. R. R. Ranasinghe, I. A. M. Sandoval, H. S. Rou, G. T. F. D. Abreu, and G. C. Alexandropoulos, “Doubly-dispersive MIMO channels with stacked intelligent metasurfaces: Modeling, parametrization, and receiver design,” *IEEE Trans. Wireless Commun.*, pp. 1–1, 2025.
54. C. Qian, Z. Wang, H. Qian, T. Cai, B. Zheng, X. Lin, Y. Shen, I. Kaminer, E. Li, and H. Chen, “Dynamic recognition and mirage using neuro-metamaterials,” *Nat. Commun.*, vol. 13, no. 1, p. 2694, May 2022.
55. C. Liu, Q. Ma, Z. J. Luo, Q. R. Hong, Q. Xiao, H. C. Zhang, L. Miao, W. M. Yu, Q. Cheng, L. Li, and T. J. Cui, “A programmable diffractive deep neural network based on a digital-coding metasurface array,” *Nat. Electron.*, vol. 5, no. 2, pp. 113–122, 2022.
56. L. Zhang, X. Q. Chen, S. Liu, Q. Zhang, J. Zhao, J. Y. Dai, G. D. Bai, X. Wan, Q. Cheng, G. Castaldi, V. Galdi, and T. J. Cui, “Space-time-coding digital metasurfaces,” *Nat. Commun.*, vol. 9, no. 1, p. 4334, Oct 2018.
57. S. P. Chepuri, N. Shlezinger, F. Liu, G. C. Alexandropoulos, S. Buzzi, and Y. C. Eldar, “Integrated sensing and communications with reconfigurable intelligent surfaces: From signal modeling to processing,” *IEEE Signal Process. Mag.*, vol. 40, no. 6, pp. 41–62, Sep. 2023.
58. D. Kompostiotis, K. Katsanos, D. Vordonis, V. Palioras, and G. C. Alexandropoulos, “Ris-aided localization and sensing,” in the book “*Smart Wireless Environments for Integrating Sensing and Communications*”. Springer Nature, Switzerland, to appear, 2026; edited by K. Meng and C. Masouros and G. C. Alexandropoulos.
59. D. Gündüz, M. A. Wigger, T.-Y. Tung, P. Zhang, and Y. Xiao, “Joint source–channel coding: Fundamentals and recent progress in practical designs,” *Proc. IEEE*, pp. 1–32, early access, 2024.
60. F. Saggese, V. Croisfelt, R. Kotaba, K. Stylianopoulos, G. C. Alexandropoulos, and P. Popovski, “On the impact of control signaling in RIS-empowered wireless communications,” *IEEE Open J. Commun. Society*, vol. 5, pp. 4383–4399, 2024.
61. G. C. Alexandropoulos, N. Shlezinger, I. Alamzadeh, M. F. Imani, H. Zhang, and Y. C. Eldar, “Hybrid reconfigurable intelligent metasurfaces: Enabling simultaneous tunable reflections and sensing for 6G wireless communications,” *IEEE Veh. Technol. Mag.*, vol. 19, no. 1, pp. 75–84, 2024.
62. Q. Zheng, M. Wen, Q. Li, G. C. Alexandropoulos, and L. Xu, “Progressive channel estimation for single-carrier communications aided by reconfigurable intelligent surfaces,” *IEEE Wirel. Commun. Lett.*, vol. 12, no. 12, pp. 1993–1997, Dec. 2023.
63. V. S. Borkar, *Basic Convergence Analysis*. Gurgaon: Hindustan Book Agency, 2008, pp. 10–20.
64. D. P. Kingma and J. Ba, “Adam: A method for stochastic optimization,” in *Proc. Int. Conf. Learn. Represent.*, San Diego, USA, 2015.

65. L. Deng, “The MNIST database of handwritten digit images for machine learning research,” *IEEE Signal Process. Mag.*, vol. 29, no. 6, pp. 141–142, 2012.
66. A. A. M. Saleh and R. Valenzuela, “A statistical model for indoor multipath propagation,” *IEEE J. Sel. Areas Commun.*, vol. 5, no. 2, pp. 128–137, 1987.
67. K. Stylianopoulos and G. C. Alexandropoulos, “Integrating stacked intelligent metasurfaces and power control for dynamic edge inference via over-the-air neural networks,” *arXiv preprint:2509.18906*, 2025.
68. H. Robbins and S. Monro, “A stochastic approximation method,” *Ann. Math. Stat.*, vol. 22, no. 3, pp. 400 – 407, 1951.
69. C. Tan, F. Sun, T. Kong, W. Zhang, C. Yang, and C. Liu, “A survey on deep transfer learning,” in *Proc. Artif. Neural Netw. Mach. Learn.*, Rhodes, Greece, 2018, pp. 270–279.
70. M. Jian, G. C. Alexandropoulos, E. Basar, C. Huang, R. Liu, Y. Liu, and C. Yuen, “Reconfigurable intelligent surfaces for wireless communications: Overview of hardware designs, channel models, and estimation techniques,” *Intell. Converged Netw.*, vol. 3, no. 1, pp. 1–32, Mar. 2022.
71. K. Stylianopoulos and G. C. Alexandropoulos, “Universal approximation with XL MIMO systems: OTA classification via trainable analog combining,” *arXiv preprint:2504.12758*, 2025.
72. M. Hua, H. Wu, and D. Gündüz, “AirCNN via reconfigurable intelligent surfaces: Architecture design and implementation,” *arXiv preprint:2510.25389*, 2025.
73. Y. Luo, D. Mengu, N. T. Yardimci, Y. Rivenson, M. Veli, M. Jarrahi, and A. Ozcan, “Design of task-specific optical systems using broadband diffractive neural networks,” *Light: Sci. Appl.*, vol. 8, no. 1, p. 112, Dec 2019.